Journal of Cosmology and Astroparticle Physics
An IOP and SISSA journal

Received: *March 5, 2026*
Revised: *June 30, 2026*
Accepted: *September 29, 2026*
Published: *November 4, 2026*

Atmospheric neutrino constraints on Lorentz invariance violation with the first six detection units of KM3NeT/ORCA

The KM3NeT collaboration

O. Adriani et al.

Full author list at the end of the paper

E-mail: adomi@km3net.de, lukas.hennig@fau.de, km3net-pc@km3net.de

Abstract: Lorentz invariance is a fundamental symmetry underlying both the Standard Model of particle physics and General Relativity. Testing its validity provides a direct means of searching for new physics emerging near the Planck scale. A search for isotropic Lorentz invariance violation using 5828 selected atmospheric-neutrino candidate events is presented. The data were collected over 1.4 years with a partial configuration of the KM3NeT/ORCA detector comprising six detection units. No evidence for such violation is found; thus, competitive constraints are set on off-diagonal isotropic Lorentz-invariance-violating coefficients of mass dimension 3. In addition, the first direct constraints on isotropic flavour-diagonal coefficient differences between the muon and tau sectors are obtained for mass dimensions 3 to 8.

Keywords: neutrino properties, solar and atmospheric neutrinos, neutrino detectors, neutrino experiments

ArXiv ePrint: 2603.04264

© 2026 The Author(s). Published by IOP Publishing Ltd on behalf of Sissa Medialab. Original content from this work may be used under the terms of the Creative Commons Attribution 4.0 licence. Any further distribution of this work must maintain attribution to the author(s) and the title of the work, journal citation and DOI.

https://doi.org/10.1088/1475-7516/2026/11/012

JCAP11(2026)012

Contents

1 Introduction **1**

2 Neutrino oscillations with isotropic Lorentz invariance violation **2**
- 2.1 Off-diagonal LIV coefficients 4
- 2.2 Diagonal LIV coefficients 5

3 The KM3NeT/ORCA detector **7**

4 Data sample and selection **7**

5 Analysis method **8**
- 5.1 Likelihood definition and confidence interval construction 8
- 5.2 Nuisance parameters 10
- 5.3 Data distribution and fit to null hypothesis 10

6 Results **11**
- 6.1 Off-diagonal coefficients 11
- 6.2 Diagonal coefficients 13
- 6.3 Interpretation of excluded LIV hypotheses 14
- 6.4 Uncertainties in the nuisance parameters 19
- 6.5 Goodness of fit and comparison to expected sensitivity 19
- 6.6 Comparison with other experiments 22

7 Conclusion **23**

A Pull distributions **24**

The KM3NeT collaboration **28**

JCAP11(2026)012

1 Introduction

Lorentz invariance is a cornerstone of modern fundamental physics and is central to our understanding of the structure of spacetime. It underlies both the Standard Model of particle physics and General Relativity, guaranteeing that the laws of physics take the same form for all inertial observers and that the outcomes of experiments are insensitive to the spatial orientation and uniform motion of the experimental setting. Despite its fundamental significance for the current understanding of spacetime, several new physics theories allow for violations of Lorentz invariance at or below the Planck scale, $M_{\mathrm{P}} \sim 10^{19}\,\mathrm{GeV}$. Examples of such theories include quantum gravity (QG) frameworks [1] such as string theory [2], loop quantum gravity [3], and doubly special relativity [4], as well as noncommutative geometry [5] and spacetime varying couplings [6]. Many of these models introduce a discretised structure of spacetime, which is inherently difficult to reconcile with continuous symmetries such as boost invariance. Testing the validity of Lorentz invariance across all experimentally accessible

regimes could reveal new insights into the microscopic structure of spacetime and eventually impose stringent constraints on QG models.

The Standard Model Extension (SME) is the most general field-theory framework that consistently incorporates both the Standard Model and General Relativity, while allowing for general violations of both Lorentz symmetry and charge, parity, time (CPT) symmetry [7]. In the SME, Lorentz invariance violating effects are expressed through tensor operators of specific mass dimension, each contracted with corresponding coefficients that quantify the magnitude of the violation, which can be constrained experimentally.

In the neutrino sector, Lorentz invariance violation (LIV) can lead to modifications of standard oscillation behaviour, potentially producing observable deviations in the energy and zenith-angle distributions of atmospheric and astrophysical neutrinos. These effects provide a promising scenario for detection through high-precision neutrino telescope experiments.

While anisotropic LIV coefficients can induce characteristic sidereal variations as the Earth rotates with respect to a preferred reference frame, the present work focuses on the isotropic sector, which preserves rotational symmetry in a preferred reference frame and therefore does not produce such modulations. Restricting the analysis to isotropic LIV substantially reduces the number of independent coefficients while retaining sensitivity to a broad class of models, making it a natural starting point for searches with neutrino oscillation experiments. More general anisotropic scenarios can be explored in future analyses. Previous searches for isotropic LIV have been carried out by Super-Kamiokande [8] and IceCube [9, 10]. No significant deviation from standard oscillations has been observed, and the results have therefore been used to place constraints on several SME coefficients.

The KM3NeT collaboration is constructing the KM3NeT/ORCA detector (Oscillation Research with Cosmics in the Abyss) [11], a deep-sea water-Cherenkov neutrino telescope positioned 40 km offshore Toulon, France, at a depth of 2450 m below sea level. KM3NeT/ORCA is specifically designed for the measurement of atmospheric neutrino oscillations in the (1−100) GeV energy range.

Atmospheric neutrino data collected over 1.4 years by a partial configuration of the KM3NeT/ORCA detector comprising six detection units (indicated in the following as ORCA6) [12] are used in this study to investigate potential LIV signatures. This is achieved through a detailed analysis of the energy-dependent spectra and angular distributions of the detected neutrino events.

The paper is organised as follows. In section 2 the relevant theoretical background is presented, with an emphasis on aspects pertinent to ORCA6. In section 3 the KM3NeT/ORCA detector is described. The data sample collected with ORCA6 and used for this study is discussed in section 4. The analysis methodology employed in this work is detailed in section 5. Finally, the results are discussed in section 6.

2 Neutrino oscillations with isotropic Lorentz invariance violation

Within the SME, the general effective Hamiltonian for neutrino propagation with LIV includes four classes of operators, leading to a rich phenomenology that can be systematically tested [7]. The limit in which only LIV operators with mass dimension $d \leq 4$ are nonzero defines the renormalisable sector, which is known to be renormalisable at least at one loop and is

JCAP11(2026)012

expected to dominate at low energies [13]. Non-renormalisable operators with $d \geq 5$ can also become relevant [7]: although the renormalisable SME sector suffices to describe physics at a low-energy scale, it becomes inadequate near high-energy scales where issues of causality and stability arise. In this regime, Planck-suppressed higher-dimension terms are expected to play an increasingly important role.

The evolution of a neutrino system in the presence of isotropic LIV is governed by the total Hamiltonian:

$$H = UH_0U^\dagger + H_{\rm M} + H_{\rm LIV}, \tag{2.1}$$

where U denotes the PMNS mixing matrix [14]. The vacuum contribution is given by

$$H_0 = \frac{1}{2E}\begin{pmatrix} 0 & 0 & 0 \\ 0 & \Delta m^2_{21} & 0 \\ 0 & 0 & \Delta m^2_{31} \end{pmatrix}, \tag{2.2}$$

which describes standard oscillations in the neutrino mass basis. The matter interaction term

$$H_{\rm M} = \pm\sqrt{2}G_{\rm F}\begin{pmatrix} N_e & 0 & 0 \\ 0 & 0 & 0 \\ 0 & 0 & 0 \end{pmatrix}, \tag{2.3}$$

is defined in the flavour basis and accounts for coherent forward scattering in ordinary matter, where the positive (negative) sign applies to neutrinos (antineutrinos). The LIV contribution is parametrised as

$$H_{\rm LIV} = \pm\begin{pmatrix} \mathring{a}^{(3)}_{ee} & \mathring{a}^{(3)}_{e\mu} & \mathring{a}^{(3)}_{e\tau} \\ \mathring{a}^{(3)*}_{e\mu} & \mathring{a}^{(3)}_{\mu\mu} & \mathring{a}^{(3)}_{\mu\tau} \\ \mathring{a}^{(3)*}_{e\tau} & \mathring{a}^{(3)*}_{\mu\tau} & \mathring{a}^{(3)}_{\tau\tau} \end{pmatrix} - E\begin{pmatrix} \mathring{c}^{(4)}_{ee} & \mathring{c}^{(4)}_{e\mu} & \mathring{c}^{(4)}_{e\tau} \\ \mathring{c}^{(4)*}_{e\mu} & \mathring{c}^{(4)}_{\mu\mu} & \mathring{c}^{(4)}_{\mu\tau} \\ \mathring{c}^{(4)*}_{e\tau} & \mathring{c}^{(4)*}_{\mu\tau} & \mathring{c}^{(4)}_{\tau\tau} \end{pmatrix} \pm E^2\mathring{a}^{(5)}_M - E^3\mathring{c}^{(6)}_M \pm E^4\mathring{a}^{(7)}_M - \ldots, \tag{2.4}$$

where $\mathring{a}^{(d)}_{\alpha\beta}$ and $\mathring{c}^{(d)}_{\alpha\beta}$, with $\alpha, \beta \in \{e, \mu, \tau\}$, denote coefficients associated with CPT-odd and CPT-even isotropic LIV operators of mass dimension d, respectively [7]. The symbols $\mathring{a}^{(d)}_M$ and $\mathring{c}^{(d)}_M$ denote Hermitian matrices of isotropic LIV coefficients, analogous to the matrices for $d = 3$ and 4 explicitly written in eq. (2.4). In the following, both cases are collectively denoted as $\mathring{k}^{(d)}_{\alpha\beta}$; odd (even) values of d correspond to CPT-odd (CPT-even) operators. For CPT-odd terms, the positive (negative) sign applies to neutrinos (antineutrinos), whereas CPT-even terms have the same sign for both neutrinos and antineutrinos.

In the SME Lagrangian density, which has mass dimension 4, each LIV term appears as the product of a coefficient and a LIV operator [7]. Therefore, if an operator has mass dimension d, the corresponding coefficient $\mathring{k}^{(d)}_{\alpha\beta}$ carries mass dimension $4 - d$. This is consistent with the $E^{d-3}\mathring{k}^{(d)}_{\alpha\beta}$ terms in the resulting effective Hamiltonian in eq. (2.4), where each contribution produces the correct mass dimension required by a Hamiltonian operator: $(d-3)+(4-d) = 1$.

It is noteworthy that the matrix $\mathring{a}^{(3)}_M$ closely resembles the structure of the propagation matrix in Non-Standard Interaction (NSI) models [15]. Although a formal correspondence exists between NSI and LIV parameters, the two frameworks affect neutrino oscillations in fundamentally different ways [16, 17]. NSI effects require neutrino propagation through

JCAP11(2026)012

matter and depend on the matter potential, whereas LIV influences oscillation probabilities even in vacuum and remains independent of matter density variations.

The LIV coefficients of a given mass dimension d can be grouped into the three off-diagonal coefficients $\mathring{k}^{(d)}_{e\mu}, \mathring{k}^{(d)}_{e\tau}, \mathring{k}^{(d)}_{\mu\tau}$ and the three diagonal coefficients $\mathring{k}^{(d)}_{ee}, \mathring{k}^{(d)}_{\mu\mu}, \mathring{k}^{(d)}_{\tau\tau}$. As described in section 4, the selected ORCA6 event sample is dominated by ν_μ-induced events and probes atmospheric neutrinos propagating across baselines up to the Earth's diameter $D_\oplus$. The following two subsections therefore focus on the impact of isotropic LIV on the muon-neutrino disappearance channel, $P(\nu_\mu \to \nu_\mu)$, in the energy range relevant for this analysis.

2.1 Off-diagonal LIV coefficients

The complex-valued LIV coefficients $\mathring{k}^{(d)}_{e\mu}, \mathring{k}^{(d)}_{e\tau}, \mathring{k}^{(d)}_{\mu\tau}$ appear on the off-diagonal of H_{LIV} in eq. (2.4). Each of these coefficients $\mathring{k}^{(d)}_{\alpha\beta}$ induces an additional mixing among the flavour states $\alpha \leftrightarrow \beta$, which is added to the mixing introduced by the off-diagonal terms in the standard-oscillation Hamiltonian $UH_0U^\dagger$ in the flavour basis. For simplicity, in the following discussion it is assumed that only one off-diagonal coefficient $\mathring{k}^{(d)}_{\alpha\beta}$ is nonzero at a time.

At sufficiently high energies, where the LIV-induced mixing $E^{d-3}\mathring{k}^{(d)}_{\alpha\beta}$ dominates the standard mixing driven by $\Delta m^2_{ij}/2E$ (see eq. (2.2)), a nonzero coefficient $\mathring{k}^{(d)}_{\alpha\beta}$ introduces transitions between the flavours $\alpha \leftrightarrow \beta$ that are absent in the standard oscillation scenario. In this high-energy limit, the oscillation phase scales as [9]

$$\phi_{\text{LIV}}(E) \propto L\, E^{d-3}\, |\mathring{k}^{(d)}_{\alpha\beta}|. \tag{2.5}$$

The first minimum in the neutrino survival probability $P(\nu_\alpha \to \nu_\alpha)$ occurs when $\phi_{\text{LIV}} = \pi/2$. For $d > 3$, this implies that the characteristic energy scale of the LIV-induced oscillations shifts to higher energies as $|\mathring{k}^{(d)}_{\alpha\beta}|$ decreases. This behaviour is illustrated in figure 1 for a neutrino traversing the Earth ($L \simeq D_\oplus$), using the $\mu\tau$ sector as an example. For $d = 3$ (left panel), the survival probability $P(\nu_\mu \to \nu_\mu)$ approaches a constant value at high energies because the phase ϕ_{LIV} in eq. (2.5) becomes energy independent. Such a predicted, nearly constant, ν_μ deficit is partly degenerate with uncertainties on the flux normalisations of atmospheric and cosmic neutrinos, which can reduce the sensitivity of high-energy neutrino telescopes like IceCube or KM3NeT/ARCA to the mass dimension 3 off-diagonal coefficients. In contrast, the KM3NeT/ORCA detector is optimised for the detection of neutrinos with energies as low as a few GeV [11], where standard oscillations induce an energy-dependent structure. In this region, a nonzero $\mathring{a}^{(3)}_{\alpha\beta}$ produces characteristic shape distortions that are exploited in this analysis, leading to stringent limits on these coefficients.

For $d > 3$ (right panel), the phase ϕ_{LIV} grows with energy and the LIV-induced oscillations move to higher energies, making the study of these coefficients better suited for analyses with higher-energy neutrino samples using, e.g., IceCube [9, 10] or KM3NeT/ARCA. For these reasons, the analysis presented in this paper focuses on constraining the three off-diagonal dimension-3 coefficients $|\mathring{a}^{(3)}_{e\mu}|$, $|\mathring{a}^{(3)}_{e\tau}|$, and $|\mathring{a}^{(3)}_{\mu\tau}|$.

JCAP11(2026)012

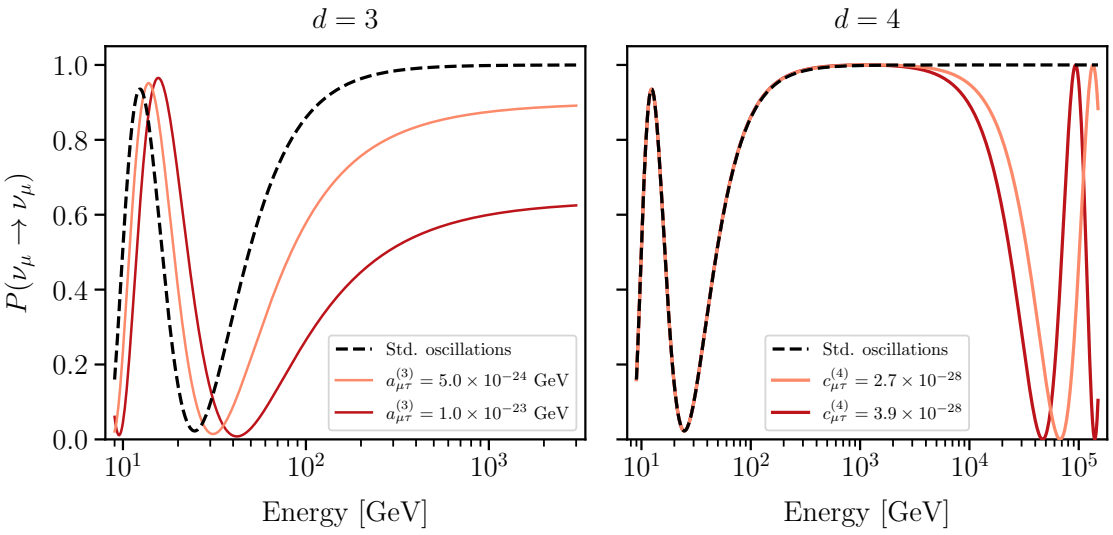


Figure 1. Muon neutrino survival probability as a function of neutrino energy. The neutrino is assumed to have traversed the Earth with a baseline $L \simeq D_\oplus$. The effect of mass dimension $d = 3$ coefficients is illustrated in the left panel using different values of $\mathring{a}^{(3)}_{\mu\tau}$ as an example. The $d > 3$ case is shown in the right panel, with $\mathring{c}^{(4)}_{\mu\tau}$ being chosen as a representative example. The values for $\mathring{a}^{(3)}_{\mu\tau}$ and $\mathring{c}^{(4)}_{\mu\tau}$ are the 90% (orange) and 99% (red) confidence level (CL) constraints reported by the IceCube collaboration in [9]. The oscillation probabilities are computed using OscProb [18].

2.2 Diagonal LIV coefficients

The real-valued diagonal part of the Hamiltonian $H_{\rm LIV}$ can be written as

$$H_{\rm LIV} = E^{d-3} \begin{pmatrix} \mathring{k}^{(d)}_{ee} & 0 & 0 \\ 0 & \mathring{k}^{(d)}_{\mu\mu} & 0 \\ 0 & 0 & \mathring{k}^{(d)}_{\tau\tau} \end{pmatrix}. \tag{2.6}$$

Oscillation probabilities are invariant under any transformation $H \to H - \lambda(E)\,\mathbb{I}$, where $\mathbb{I}$ is the identity matrix, since this transformation only adds a global phase. Hence, it is allowed to subtract the term $E^{d-3}\mathring{k}^{(d)}_{\tau\tau}$ from the diagonal of the Hamiltonian. This leaves two independent diagonal combinations,

$$H_{\rm LIV} = E^{d-3} \begin{pmatrix} \mathring{k}^{(d)}_{ee} - \mathring{k}^{(d)}_{\tau\tau} & 0 & 0 \\ 0 & \mathring{k}^{(d)}_{\mu\mu} - \mathring{k}^{(d)}_{\tau\tau} & 0 \\ 0 & 0 & 0 \end{pmatrix}. \tag{2.7}$$

After including matter effects relevant for atmospheric neutrinos traversing the Earth, the interaction Hamiltonian in the flavour basis becomes

$$H_{\rm I} = H_{\rm M} + H_{\rm LIV} = \begin{pmatrix} V_e + E^{d-3}\,(\mathring{k}^{(d)}_{ee} - \mathring{k}^{(d)}_{\tau\tau}) & 0 & 0 \\ 0 & E^{d-3}\,(\mathring{k}^{(d)}_{\mu\mu} - \mathring{k}^{(d)}_{\tau\tau}) & 0 \\ 0 & 0 & 0 \end{pmatrix}. \tag{2.8}$$

JCAP11(2026)012

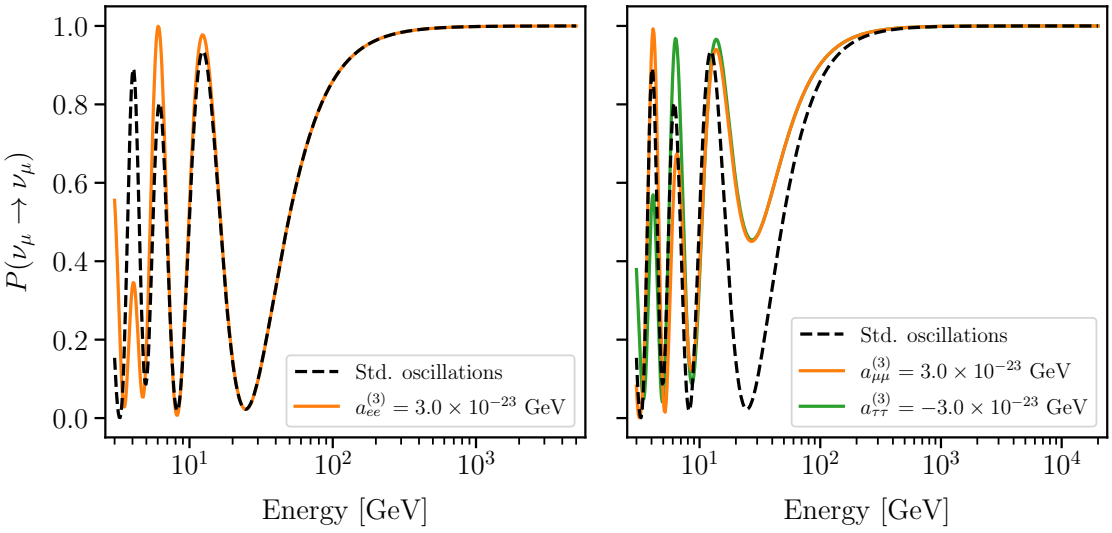


Figure 2. Muon neutrino survival probability as a function of neutrino energy. The neutrino is assumed to have traversed the Earth with a baseline $L \simeq D_\oplus$. The left panel shows the effect of a nonzero $\mathring{k}_{ee}^{(d)}$, while the right panel illustrates the effect of a nonzero $\mathring{k}_{\mu\mu}^{(d)}$ and $-\mathring{k}_{\tau\tau}^{(d)}$, respectively. Mass dimension $d = 3$ has been chosen as a representative example, using a coefficient value suitable for an illustration of LIV effects. The oscillation probabilities are computed using OscProb [18].

First, a nonzero $\mathring{k}_{ee}^{(d)}$ with $\mathring{k}_{\mu\mu}^{(d)} = \mathring{k}_{\tau\tau}^{(d)} = 0$ is considered. Equation (2.8) shows that $\mathring{k}_{ee}^{(d)}$ enters as an additive contribution to the ee entry of the Hamiltonian matrix, i.e., it effectively shifts the standard matter potential V_e. Since the contribution scales as E^{d-3}, the effective shift of V_e is energy independent for $d = 3$ and energy dependent for $d > 3$. As illustrated in figure 2 (left panel), a nonzero $\mathring{k}_{ee}^{(d)}$ mainly affects $P(\nu_\mu \to \nu_\mu)$ in the few-GeV region, where it produces both positive and negative deviations with respect to the standard oscillation curve. After folding in the finite energy resolution, these deviations largely average out, and the limited statistics corresponding to the ORCA6 exposure does not allow for resolving the remaining effect. Therefore, $\mathring{k}_{ee}^{(d)}$ is not constrained in this analysis.

Next, a nonzero $\mathring{k}_{\mu\mu}^{(d)}$ with $\mathring{k}_{ee}^{(d)} = \mathring{k}_{\tau\tau}^{(d)} = 0$ is considered. In this case, $\mathring{k}_{\mu\mu}^{(d)}$ acts as an additional potential in the $\mu\mu$ entry of eq. (2.8). As shown in figure 2 (right panel), a nonzero $\mathring{k}_{\mu\mu}^{(d)}$ produces a significant modification of $P(\nu_\mu \to \nu_\mu)$ in the energy range relevant for this analysis. Therefore, the analysis is sensitive to the LIV effects induced by $\mathring{k}_{\mu\mu}^{(d)}$.

Finally, a nonzero $\mathring{k}_{\tau\tau}^{(d)}$ with $\mathring{k}_{ee}^{(d)} = \mathring{k}_{\mu\mu}^{(d)} = 0$ is considered. As can be seen in eq. (2.8), a nonzero $\mathring{k}_{\tau\tau}^{(d)}$ simultaneously induces an effective negative shift in both the ee and $\mu\mu$ entries, i.e. it combines the qualitative features discussed above for $\mathring{k}_{ee}^{(d)}$ and $\mathring{k}_{\mu\mu}^{(d)}$. In the energy range relevant for this analysis, the dominant impact on $P(\nu_\mu \to \nu_\mu)$ arises from the effective shift of the $\mu\mu$ entry, while the accompanying shift of the ee entry mainly affects the few-GeV region. Consequently, the effects of varying $\mathring{k}_{\mu\mu}^{(d)}$ and of varying $-\mathring{k}_{\tau\tau}^{(d)}$ appear nearly degenerate in figure 2 (right panel) at energies $> 10\,\text{GeV}$. For this reason, constraints on the diagonal combinations $(\mathring{k}_{\mu\mu}^{(d)} - \mathring{k}_{\tau\tau}^{(d)})$ are reported, which for brevity are denoted as $\mathring{k}_{\mu\mu-\tau\tau}^{(d)}$.

JCAP11(2026)012

These diagonal combinations enter the Hamiltonian as an effective potential term proportional to $E^{d-3}\,\mathring{k}^{(d)}_{\mu\mu-\tau\tau}$. Since the energy dependence becomes stronger with increasing d, the same effective potential size in a fixed energy range can be produced by progressively smaller coefficient values as d increases. This scaling behaviour explains why the ORCA6 data sample retains sensitivity to diagonal coefficients of higher mass dimension. Consequently, the diagonal combination $\mathring{k}^{(d)}_{\mu\mu-\tau\tau}$ is constrained from mass dimension $d = 3$ up to $d = 8$.

3 The KM3NeT/ORCA detector

KM3NeT/ORCA is a deep-sea water-Cherenkov neutrino telescope designed to measure atmospheric neutrino oscillations in the 1–100 GeV energy range. When neutrinos interact within or near the instrumented volume, they generate secondary charged particles that induce Cherenkov radiation, which is detected by a three-dimensional array of digital optical modules [19]. Each module houses 31 photomultiplier tubes (PMTs) alongside readout electronics and calibration sensors for precise positioning, orientation, and timing. The optical modules are arranged vertically along detection units each comprising 18 modules, which are anchored to the seabed and maintained in approximate vertical position by buoyancy distributed in the optical modules and a top buoy, enabling accurate reconstruction of neutrino energy and arrival direction. KM3NeT/ORCA is deployed in a modular configuration with detection units spaced horizontally at approximately 20 m intervals and optical modules separated vertically by 9 m along each unit. The completed detector will feature more than a hundred detection units, creating a dense optical array optimised for high-precision atmospheric neutrino oscillation measurements and neutrino mass ordering determination.

The data used in this analysis were collected with ORCA6, which refers to the configuration of the KM3NeT/ORCA detector comprising the first six deployed detection units. This configuration was operated from January 2020 to November 2021. A top view of the ORCA6 detector layout is shown in figure 2 of [12].

4 Data sample and selection

The collected data were filtered according to quality criteria for environmental conditions and the stability of the data-taking, resulting in a dataset with 510 days of livetime and 433 kton-years of exposure [12].

The deep-sea environment provides a constant background of optical photons from the radioactive decay of ^{40}K and from bioluminescence caused by microorganisms. This dominating background is reduced by applying trigger algorithms to search for causal correlations between the measured PMT signals. The remaining background events due to random coincidences are further suppressed to a negligible sub-percent level by applying selection cuts on quality criteria based on the output of reconstruction algorithms.

At this stage of the selection, muons created in the atmosphere dominate the sample by seven orders of magnitude over the neutrino events. The muon contamination is reduced in two steps. The first step exploits the fact that the Earth is transparent for neutrinos at the energies considered in this analysis, while it is opaque to muons. By only selecting events reconstructed as up-going in the detector, the Earth is used as a shield against the atmospheric

JCAP11(2026)012

muon flux. Furthermore, a boosted decision tree (BDT) is trained to remove remaining muon events that are misreconstructed as up-going. The corresponding classifier output, referred to as the atmospheric muon score, is shown in figure 3 (left) of [12]. Applying a selection on this score reduces the atmospheric muon contamination below 2% while retaining 60% of the estimated neutrino signal of the previous step.

The last selection level differentiates between the two main event topologies, which are referred to as track-like and shower-like events. Track-like events are predominantly caused by muon neutrinos undergoing a charged-current (CC) interaction resulting in the creation of a muon. This charged particle induces the emission of Cherenkov radiation in the water while propagating tens to hundreds of metres, resulting in an elongated, track-like light signal in the detector. In contrast, shower-like events are mainly caused by CC interactions of electron neutrinos and tau neutrinos as well as neutral-current (NC) interactions induced by all flavours. These interactions produce electromagnetic and hadronic showers emitting light along a distance which is small compared to the distance between optical modules, resulting in the measurement of a nearly spherically-distributed light signal.

The discrimination between track- and shower-like events is performed with a second BDT. The corresponding classifier output, referred to as the track score, is shown in figure 3 (right) of [12]. Based on the atmospheric muon score and track score, three event classes are defined, which are termed High Purity Tracks (HPT), Low Purity Tracks (LPT), and Showers. These classes are optimised for sensitivity on standard oscillation parameters and are used for all ORCA6 analyses [12, 15, 20–23]. The corresponding energy and zenith-angle reconstruction resolutions for the three event classes are shown in figure 3.

The best fit to the standard oscillation hypothesis estimates 5828 observed events summed over the three classes. The muon neutrino and antineutrino fraction is 95% for the HPT class, 90% for the LPT class, and 46% for the Showers class, while the atmospheric muon contaminations are 0.4%, 4%, and 1%, respectively. Further details on the data sample used in this analysis can be found in [12].

5 Analysis method

5.1 Likelihood definition and confidence interval construction

The detected events in each class are binned in the logarithm of the reconstructed energy, $\log\left(E_{\text{reco}}/\text{GeV}\right)$, and in the reconstructed cosine of the zenith angle, $\cos\theta$. Ten equally-spaced bins are used for the reconstructed $\cos\theta \in [-1, 0]$, with -1 (0) representing vertically upgoing (horizontal) events. The reconstructed energy is binned into 15 log-spaced bins with $E_{\text{reco}} \in [2\,\text{GeV}, 1\,\text{TeV}]$. For the HPT and LPT classes, the highest-energy bin spanning $E_{\text{reco}} \in [100\,\text{GeV}, 1\,\text{TeV}]$ is excluded from the fit.

The histograms obtained from observed events are compared to templates obtained using Monte Carlo (MC) simulated events that are reweighted according to the hypothesis under test. Point estimates for the LIV-parameters are obtained through Maximum Likelihood Estimation. The negative log-likelihood used in this analysis is

$$-2\log\mathcal{L} = \sum_i 2\left[\beta_i N_i^{\text{exp}} - N_i^{\text{obs}} + N_i^{\text{obs}}\log\left(\frac{N_i^{\text{obs}}}{\beta_i N_i^{\text{exp}}}\right)\right] + \frac{(\beta_i - 1)^2}{\sigma_{\beta_i}^2} + \sum_k \left(\frac{\eta_k - \langle\eta_k\rangle}{\sigma_{\eta_k}}\right)^2. \quad (5.1)$$

JCAP11(2026)012

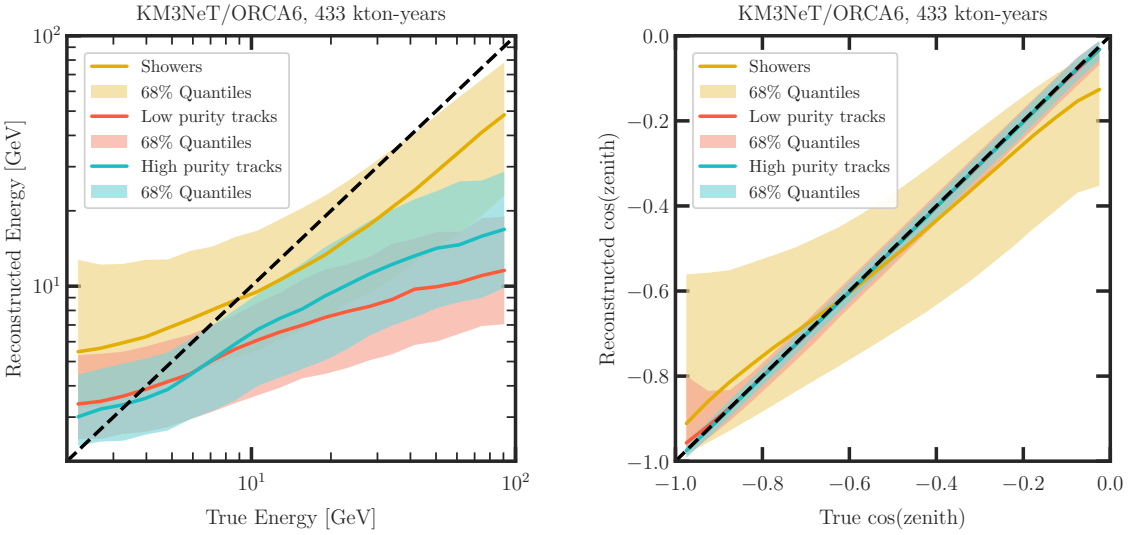


Figure 3. Reconstruction performance for the three event classes used in this analysis. Left: reconstructed energy as a function of the true neutrino energy. [12] Right: reconstructed $\cos\theta$ as a function of the true value. The solid lines show the median reconstructed quantities for High Purity Tracks (blue), Low Purity Tracks (red), and Showers (yellow), while the shaded bands indicate the corresponding central 68% quantile ranges. The dashed diagonal lines correspond to perfect reconstruction.

The index i in the first sum runs over all the aforementioned bins in reconstruction space, computing the Poisson likelihood that a bin with N^{exp} expected events has N^{obs} observed events. The second term treats the limited MC statistics by introducing normally-distributed coefficients β_i, following the Barlow-Beeston light method [24, 25]. The impact of the MC statistical uncertainties was checked explicitly for representative LIV coefficients and was found to affect the resulting limits only at the percent level. Therefore, MC statistical uncertainties do not represent a limiting contribution to the sensitivity of this analysis. The index k in the last sum runs over nuisance parameters, which treat systematic uncertainties from various sources. They are further discussed in section 5.2. The available information on the range of a nuisance parameter η_k is modelled using a Gaussian prior with mean $\langle\eta_k\rangle$ and standard deviation σ_{η_k}. In the case of no available information, the nuisance parameter is allowed to vary freely and does not enter the sum over the index k.

In order to construct confidence intervals, a test statistic (TS) has to be chosen. This analysis uses the likelihood ratio defined as

$$-2\Delta\log\mathcal{L}(\omega_0) = -2\log\left(\frac{\mathcal{L}(\omega_0,\hat{\hat{\vec{\eta}}})}{\mathcal{L}(\hat{\omega},\hat{\vec{\eta}})}\right), \tag{5.2}$$

where ω denotes the LIV parameter that is allowed to vary and $\vec{\eta}$ denotes the vector of nuisance parameters. The hat over $\hat{\omega}$ and $\hat{\vec{\eta}}$ denotes the point estimate that minimises the negative log-likelihood. The implementation of this minimisation procedure is based on the MINUIT library [26]. For the construction of confidence intervals, a grid of LIV parameter

JCAP11(2026)012

values is scanned. For each LIV parameter value ω_0 on this grid, the negative log-likelihood $-2\log\mathcal{L}(\omega_0, \vec{\eta})$ is minimised with ω_0 kept fixed, resulting in a profiled best fit vector $\hat{\hat{\vec{\eta}}}$ for the nuisance parameters. According to Wilks' theorem [27], the distribution of this TS can be approximated by a χ^2-distribution with one degree of freedom, which is used for the construction of confidence intervals. A Feldman-Cousins construction [28] is not used here, since the required pseudo-experiment ensembles for each scanned LIV coefficient would be computationally too costly given the large number of parameters studied in this analysis.

5.2 Nuisance parameters

Fifteen nuisance parameters are used to handle systematic uncertainties arising from oscillation parameters, cross sections and selection efficiencies, detector characteristics, and the atmospheric neutrino flux. A complete list of the nuisance parameters can be found in table 1. This section gives a brief overview of the nuisance parameters, with a comprehensive explanation available in [12].

The uncertainties on standard oscillation parameters are taken into account by letting Δm^2_{31} and θ_{23} vary freely during the fit. Other oscillation parameters have a negligible effect on the analysis and thus are fixed to their best fit values from NuFit 5.0 with Super-Kamiokande data assuming normal ordering [29].

The overall normalisation factor f_{all} is applied as a common scaling factor to the number of expected selected events in all classes. In addition, the relative normalisation factors f_{HPT} and f_{S} are applied to scale the numbers of expected selected events in the HPT and Shower classes, respectively, relative to this global scaling. This parameterisation allows for a combined treatment of the uncertainties in the neutrino cross sections and the selection efficiencies. The uncertainty in the estimation of the remaining atmospheric muon background is modelled using a normalisation f_μ. Event selection uncertainties of CC ν_τ events and all-flavour NC events are analogously modelled using scaling factors $f_{\tau\text{CC}}$ and f_{NC} applied to these respective types of events.

A nuisance parameter E_s is introduced to shift the absolute energy scale of the detector, which accounts for uncertainties in the optical properties of the detector medium, the PMT efficiencies, and hadronic showers. Furthermore, the scaling factor f_{HE} is applied to high-energy events, accounting for different assumptions made during the simulated light propagation of low-energy and high-energy events in seawater.

The nominal atmospheric neutrino flux used in this analysis is the HKKMS 2015 model [30] averaged over the azimuth and evaluated at the Fréjus site. The spectral index δ_γ models uncertainties in the steepness of the energy spectrum, while the parameter δ_θ relates to uncertainties in the zenith distribution of the atmospheric neutrino flux. The remaining three nuisance parameters model uncertainties in the $\nu/\bar{\nu}$ and ν_μ/ν_e ratios.

5.3 Data distribution and fit to null hypothesis

Figure 4 shows the observed event distributions together with the expectation obtained after fitting the null hypothesis corresponding to standard neutrino oscillations. The distributions are shown separately for the HPT, LPT, and Showers event classes in the two-dimensional analysis space spanned by reconstructed energy and reconstructed zenith angle.

JCAP11(2026)012

Parameter		Uncertainty
Oscillation parameters:		
Mass-squared difference	Δm^2_{31}	—
Mixing angle	θ_{23}	—
Normalisations:		
High-purity tracks	f_{HPT}	—
Showers	f_{S}	—
Overall	f_{all}	—
Atm. muon background	f_{μ}	—
$\nu_\tau + \bar{\nu}_\tau$ CC normalisation	$f_{\tau\mathrm{CC}}$	$\pm 20\%$
NC normalisation	f_{NC}	$\pm 20\%$
Detector characteristics:		
Energy scale	E_s	$\pm 9\%$
High-energy light yield	f_{HE}	$\pm 50\%$
Atmospheric neutrino flux:		
Spectral index	δ_γ	± 0.3
Ratio up-going to horizontal ν	δ_θ	$\pm 2\%$
$\nu_\mu/\bar{\nu}_\mu$ ratio	$s_{\mu\bar{\mu}}$	$\pm 5\%$
$\nu_e/\bar{\nu}_e$ ratio	$s_{e\bar{e}}$	$\pm 7\%$
ν_μ/ν_e ratio	$s_{e\mu}$	$\pm 2\%$

Table 1. The nuisance parameters and their prior uncertainties as defined in [12]. Parameters without a value in the "Uncertainty" column are allowed to vary freely during the fit.

The bottom row of figure 4 shows the per-bin statistical contribution to the likelihood function defined in equation (5.1) without the nuisance-parameter penalty terms. No individual region of the analysis space is observed to dominate the fit, with contributions distributed across many bins in all three event classes.

A detailed discussion of the null-hypothesis fit, including the best-fit values of the oscillation and nuisance parameters, the estimated event composition of the three event classes, the impact of systematic uncertainties, and the goodness-of-fit, can be found in [12].

6 Results

The analysis has been performed individually for all off-diagonal coefficients of mass dimension 3 and for the diagonal coefficient combinations $\mathring{k}^{(d)}_{\mu\mu} - \mathring{k}^{(d)}_{\tau\tau}$ with $3 \leq d \leq 8$, i.e., only one LIV coefficient is allowed to be nonzero in each fit. No significant LIV effect has been found. Hence, in this section the upper limits obtained with the ORCA6 data sample are reported and compared to limits set by other experiments.

6.1 Off-diagonal coefficients

In the SME, the off-diagonal coefficients $\mathring{a}^{(3)}_{\alpha\beta}$ are complex and can be written as $\mathring{a}^{(3)}_{\alpha\beta} = |\mathring{a}^{(3)}_{\alpha\beta}|\, e^{i\delta^{(3)}_{\alpha\beta}}$. The impact of the complex phase has been assessed by performing two-dimensional

JCAP11(2026)012

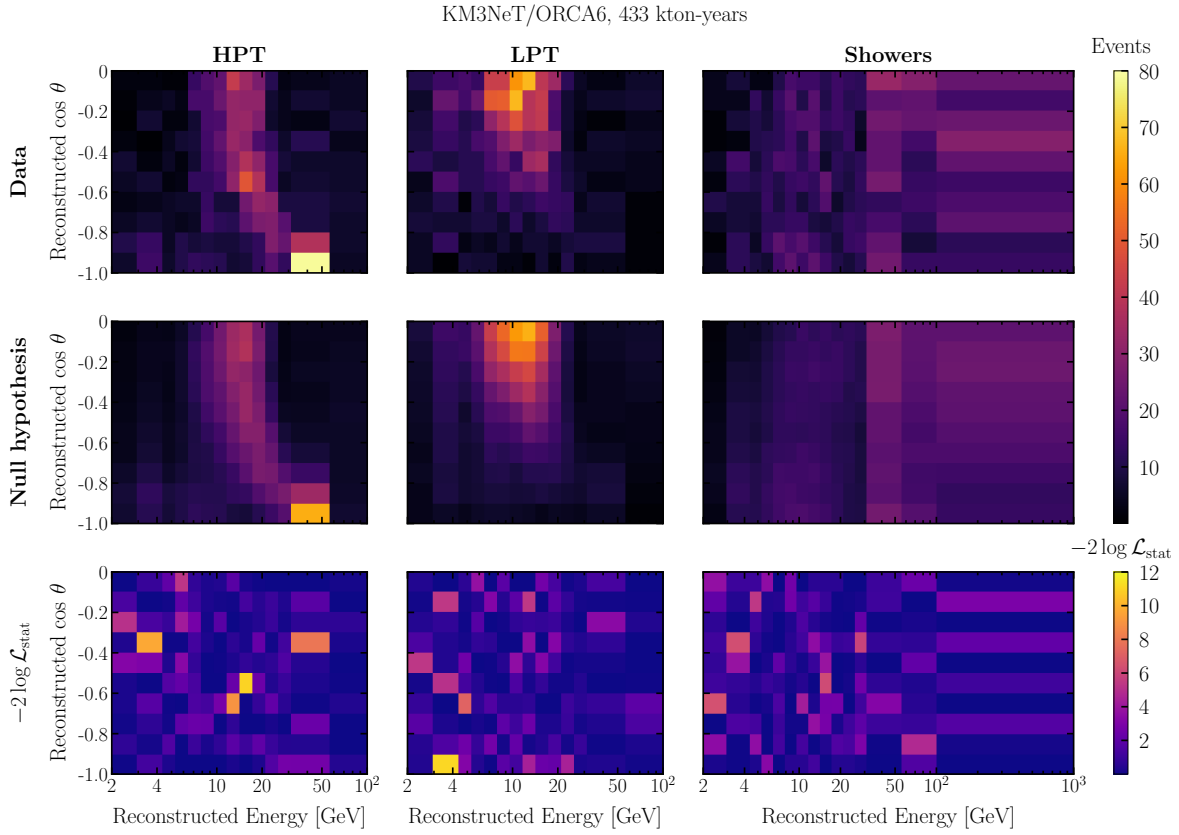


Figure 4. Observed and expected reconstructed event distributions for the ORCA6 dataset in the three particle-identification classes used in the analysis: HPT (left column), LPT (centre column), and Showers (right column). The top row shows the observed data distributions, while the middle row shows the expected distributions after fitting the null hypothesis corresponding to standard neutrino oscillations. The bottom row displays the per-bin statistical contribution to the likelihood $-2\log\mathcal{L}_{\text{stat}}$, corresponding to equation (5.1) without the nuisance-parameter penalty terms.

sensitivity scans using the test statistic in eq. (5.2). Assuming Wilks' theorem [27], the test statistic follows a χ^2 distribution with two degrees of freedom, which is used to draw the 95% CL contour in figure 5. Along the 95% CL contour, the inferred upper limit on $|\mathring{a}^{(3)}_{\mu\tau}|$ varies at the $\sim 15\%$ level when scanning over the phase $\delta^{(3)}_{\mu\tau}$ (upper left panel). This dependence is sufficiently weak that the analysis could be simplified to one-dimensional scans by fixing the phase. For $|\mathring{a}^{(3)}_{e\mu}|$ and $|\mathring{a}^{(3)}_{e\tau}|$ (upper right and bottom panel), the corresponding variation along the 95% CL contour is only at the few-percent level, so the choice of a fixed phase has a negligible impact within the sensitivity of this dataset. Therefore, $\delta^{(3)}_{\alpha\beta} = 0$ is fixed for all off-diagonal coefficients and only the magnitudes $|\mathring{a}^{(3)}_{\alpha\beta}|$ are constrained. For $\mu\tau$ this corresponds to a conservative choice, while for $e\mu$ and $e\tau$ the effect of the phase choice is negligible.

Likelihood ratio scans of the three off-diagonal coefficients are shown in figure 6. The derived 95% and 99% CL upper limits and best-fit points are listed in table 2.

JCAP11(2026)012

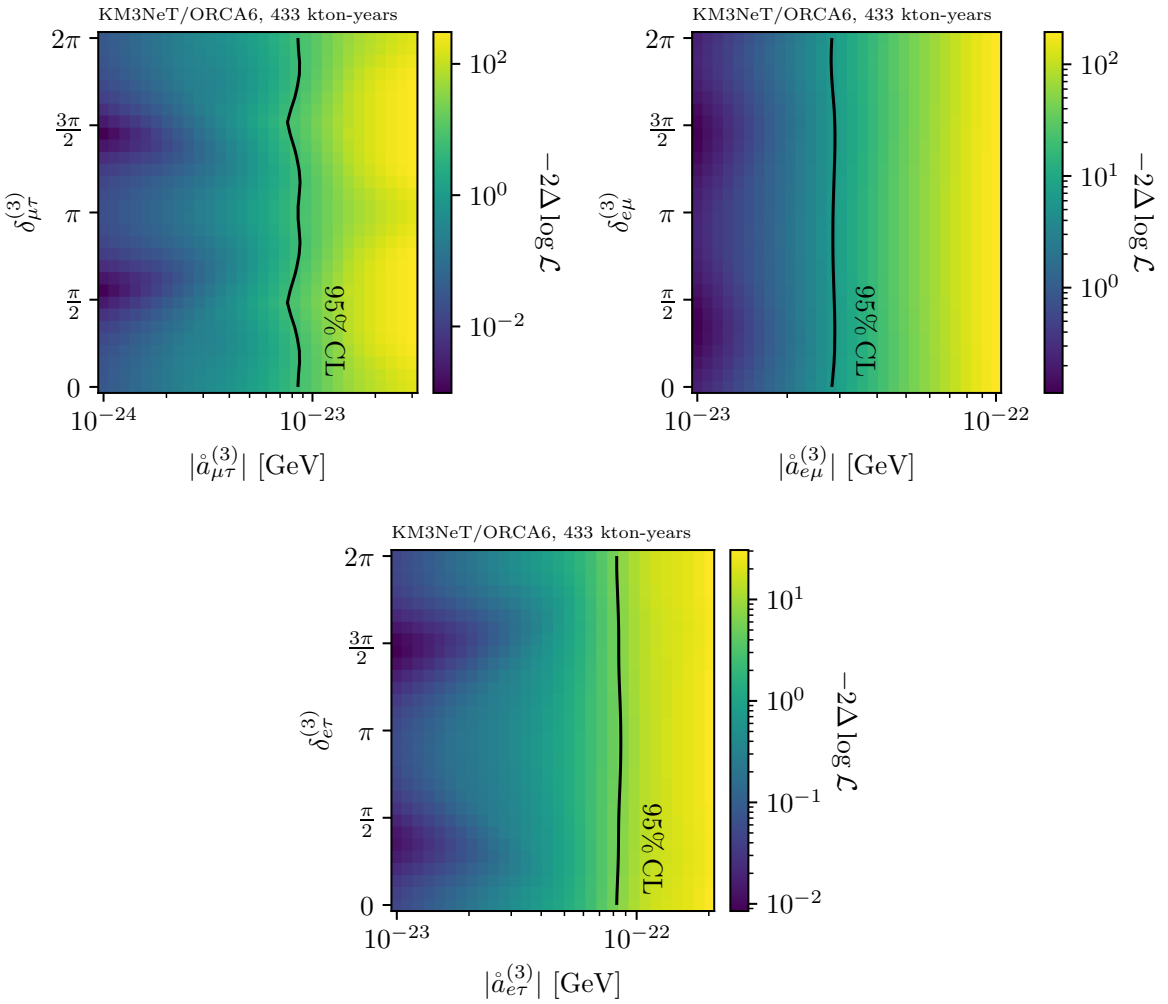


Figure 5. Two-dimensional sensitivities for the magnitude and phase of $d = 3$ off-diagonal coefficients. The 95% confidence level contour is shown in each panel.

LIV coefficient	Unit	Best fit	95% CL	99% CL
$\lvert\mathring{a}^{(3)}_{\mu\tau}\rvert$	10^{-23} GeV	9.44×10^{-2}	0.48	0.57
$\lvert\mathring{a}^{(3)}_{e\mu}\rvert$	10^{-23} GeV	4.97×10^{-5}	2.53	3.02
$\lvert\mathring{a}^{(3)}_{e\tau}\rvert$	10^{-23} GeV	4.22×10^{-10}	4.70	5.75

Table 2. Best fits and upper limits for the isotropic LIV coefficients $|\mathring{a}^{(3)}_{\mu\tau}|$, $|\mathring{a}^{(3)}_{e\mu}|$, and $|\mathring{a}^{(3)}_{e\tau}|$.

6.2 Diagonal coefficients

The likelihood-ratio contours of the diagonal coefficients are shown in figure 7. The resulting limits are listed, together with the corresponding best-fit points, in table 3.

The likelihood-ratio contours for the diagonal coefficient differences $\mathring{k}^{(d)}_{\mu\mu} - \mathring{k}^{(d)}_{\tau\tau}$ are nearly symmetric around zero. This behaviour can be understood from an idealised two-flavour picture in the $\nu_\mu - \nu_\tau$ sector, which provides useful intuition for the atmospheric $\nu_\mu \to \nu_\tau$ oscillation behaviour. In this picture, the diagonal coefficient difference acts as an additional

JCAP11(2026)012

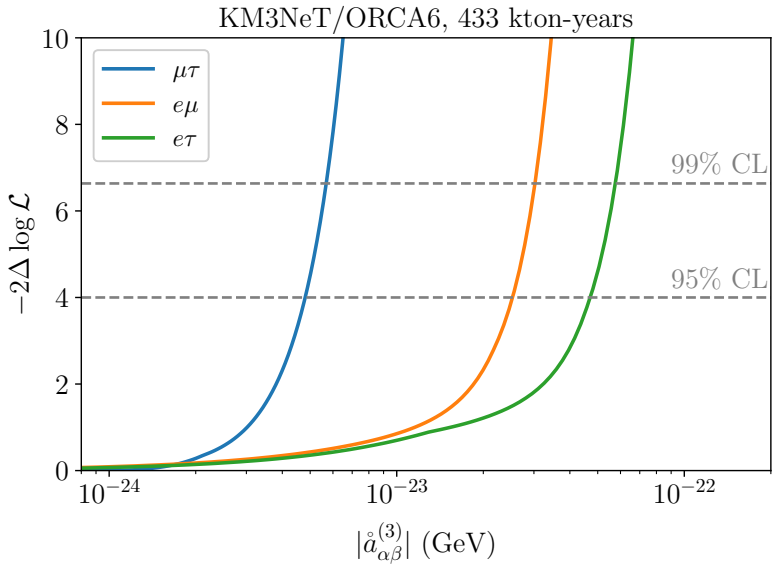


Figure 6. Likelihood ratio scans for $d = 3$ off-diagonal coefficients. The intersections with the dashed lines define the upper limits.

flavour-dependent splitting between ν_μ and ν_τ, analogous in form to the role of the matter potential in matter-modified oscillations. In the two-flavour vacuum limit with maximal atmospheric mixing, $\theta_{23} = 45°$, the ν_μ survival probability depends only on the magnitude of this splitting. Therefore, changing the sign of the coefficient leaves the probability unchanged in this idealised limit.

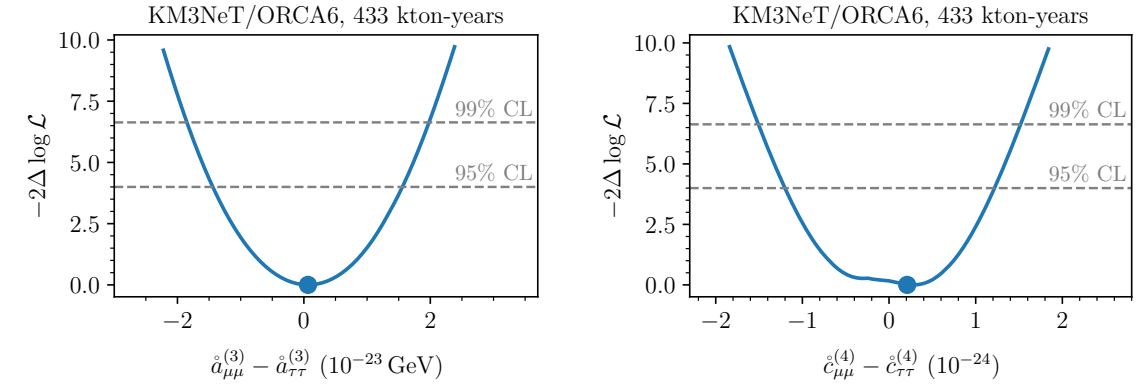
The symmetry is only approximate in the full analysis. It is already slightly broken in the two-flavour picture if θ_{23} is not exactly maximal, and further asymmetries arise from the full three-flavour treatment and matter effects during propagation through the Earth. For CPT-odd coefficients, the LIV term enters the neutrino and antineutrino Hamiltonians with opposite signs, as shown in eq. (2.4). Since neutrinos and antineutrinos are not distinguished in the analysis and contribute with different weights due to flux and cross-section differences, reversing the sign of a CPT-odd coefficient does not leave the expected event distribution exactly unchanged.

Nevertheless, the approximate sign symmetry is still visible in figure 7. In several panels, two local minima appear on opposite sides of zero, which can be understood as a consequence of this approximate symmetry.

6.3 Interpretation of excluded LIV hypotheses

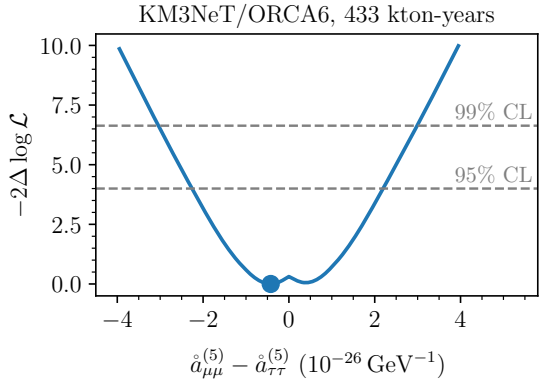
To gain insight into the physical origin of the constraints obtained in this analysis, several representative LIV coefficients are examined in more detail. Figure 8 shows the modifications of the atmospheric ν_μ survival probability induced by four selected LIV coefficients fixed to their respective 99% CL excluded values. Figure 9 shows the statistical per-bin contribution to the test statistic. Together, these figures illustrate the regions of the analysis space that are primarily responsible for the exclusion of the selected LIV coefficients.

JCAP11(2026)012

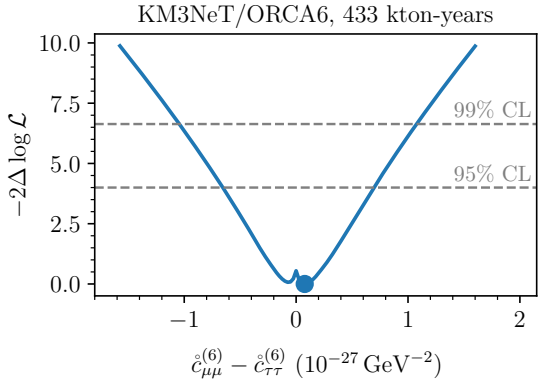


(a) $d = 3$.

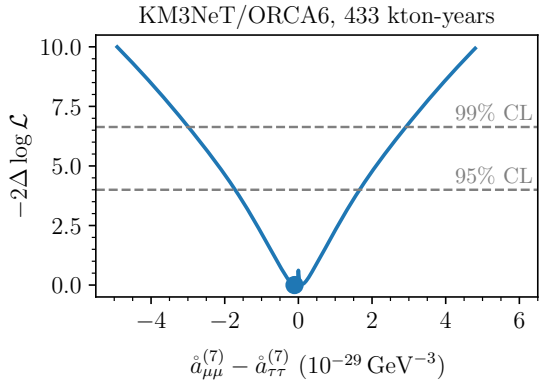
(b) $d = 4$.



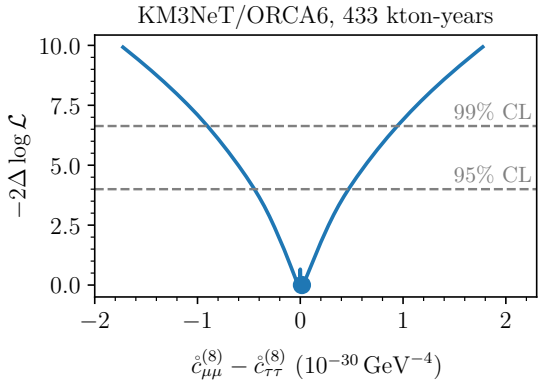
(c) $d = 5$.



(d) $d = 6$.



(e) $d = 7$.



(f) $d = 8$.

Figure 7. Likelihood-ratio scans for diagonal coefficient combinations across $d = 3, \ldots, 8$. The blue dot in each panel indicates the respective best-fit point for that dimension. The intersections with the dashed lines define the upper limits.

JCAP11(2026)012

LIV coefficient	Unit	Best fit	95% CL		99% CL	
			low	high	low	high
$\mathring{a}^{(3)}_{\mu\mu} - \mathring{a}^{(3)}_{\tau\tau}$	10^{-23} GeV	0.07	−1.44	1.56	−1.85	1.98
$\mathring{c}^{(4)}_{\mu\mu} - \mathring{c}^{(4)}_{\tau\tau}$	10^{-24}	0.28	−1.20	1.22	−1.51	1.52
$\mathring{a}^{(5)}_{\mu\mu} - \mathring{a}^{(5)}_{\tau\tau}$	10^{-26} GeV^{-1}	−0.48	−2.26	2.20	−3.04	2.99
$\mathring{c}^{(6)}_{\mu\mu} - \mathring{c}^{(6)}_{\tau\tau}$	10^{-27} GeV^{-2}	0.08	−0.65	0.69	−1.04	1.08
$\mathring{a}^{(7)}_{\mu\mu} - \mathring{a}^{(7)}_{\tau\tau}$	10^{-29} GeV^{-3}	−0.10	−1.72	1.66	−2.99	2.92
$\mathring{c}^{(8)}_{\mu\mu} - \mathring{c}^{(8)}_{\tau\tau}$	10^{-31} GeV^{-4}	0.16	−4.46	4.69	−9.04	9.44

Table 3. Best fits and upper limits for the diagonal LIV differences $\mathring{k}^{(d)}_{\mu\mu} - \mathring{k}^{(d)}_{\tau\tau}$ for $d = 3, \ldots, 8$.

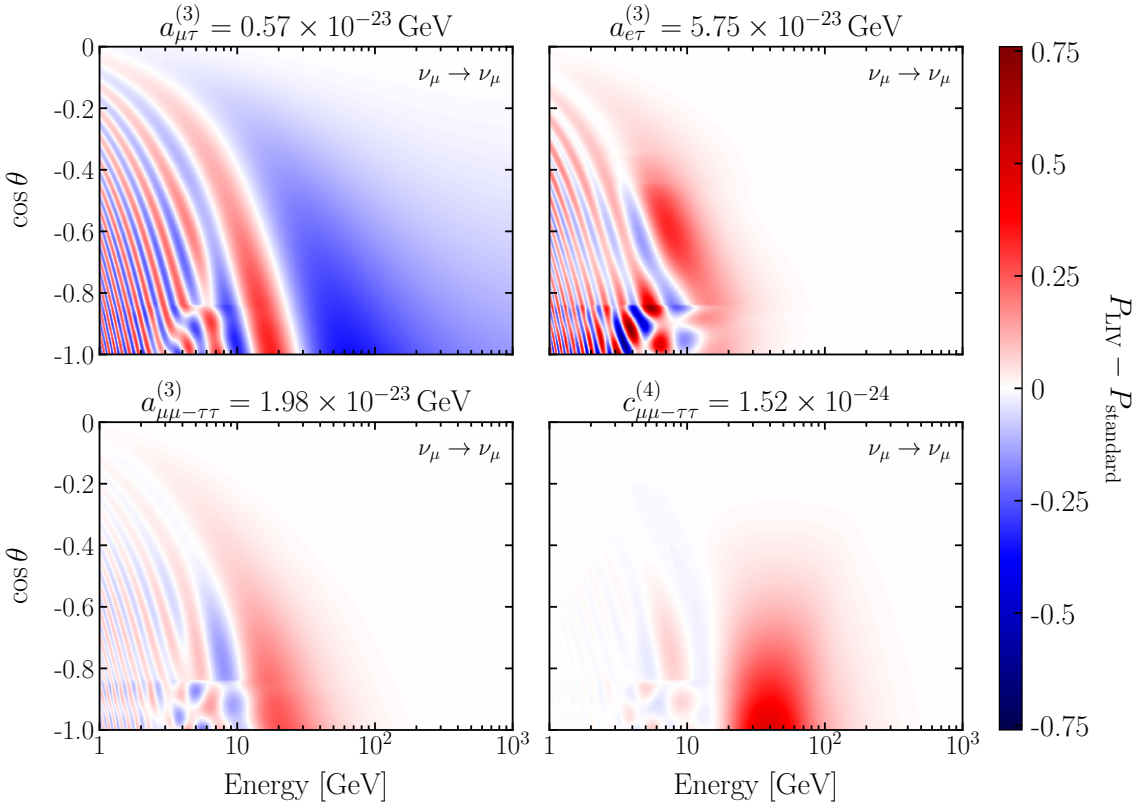


Figure 8. Oscillograms illustrating the effect of selected LIV coefficients on the atmospheric ν_μ survival probability. The panels show the differences $P_{\rm LIV}(\nu_\mu \to \nu_\mu) - P_{\rm standard}(\nu_\mu \to \nu_\mu)$ as functions of neutrino energy and zenith angle, where $P_{\rm LIV}$ and $P_{\rm standard}$ denote the oscillation probabilities in the presence and absence of LIV, respectively. Red (blue) regions correspond to an enhanced (suppressed) ν_μ survival probability relative to the standard oscillation scenario. The LIV coefficients are fixed to their respective 99% confidence-level excluded values obtained in this analysis. The oscillation probabilities are computed using OscProb [18].

JCAP11(2026)012

For $\mathring{a}^{(3)}_{\mu\tau}$, the LIV term introduces additional $\nu_\mu - \nu_\tau$ mixing. At the value shown in figure 8, the resulting modification of the oscillation probability decreases the ν_μ survival probability relative to the standard oscillation scenario for vertically upgoing neutrinos above approximately 30 GeV. At lower energies, the LIV-induced modifications show a more rapidly varying structure, which is partially smeared by the finite detector resolutions and therefore provides less discrimination with respect to the standard oscillation expectation. The resulting tension therefore arises primarily from the high-energy region of the HPT sample, where the LIV hypothesis predicts fewer events than observed. In particular, the largest contribution originates from the highest-populated bin in the entire analysis sample, which is located in the high-energy, vertically upgoing region of the HPT class. In the particular dataset used in this analysis, this bin exhibits an excess of observed events relative to the best-fitting standard oscillation hypothesis (see figure 4), thereby further increasing the tension.

For $\mathring{a}^{(3)}_{e\tau}$, the exclusion mechanism is more subtle. At sufficiently high energies, the coefficient primarily induces $\nu_e \leftrightarrow \nu_\tau$ oscillations and therefore has no direct impact on the oscillation channels to which the HPT and LPT classes are most sensitive. However, at lower energies the LIV contribution to the Hamiltonian becomes comparable to the standard oscillation contributions and modifies the full three-flavour mixing pattern. As a consequence, the LIV-induced modification pattern shown in figure 8 shows sizeable distortions of the ν_μ survival probability, most notably an enhancement around $E \sim 10\,\mathrm{GeV}$ and $\cos\theta \sim -0.6$. These distortions generate tension primarily in the HPT and LPT classes, where the LIV scenario predicts an excess of track-like events. In contrast, the Showers class exhibits only a weak sensitivity to this coefficient and even shows a slight preference for the LIV scenario in some regions of the analysis space. The exclusion of $\mathring{a}^{(3)}_{e\tau}$ therefore arises predominantly from the measurable distortions of the ν_μ survival probability, rather than from direct sensitivity to $\nu_e \leftrightarrow \nu_\tau$ transitions. Since such distortions become sizeable only for comparatively large values of $\mathring{a}^{(3)}_{e\tau}$, the resulting constraint is weaker than for $\mathring{a}^{(3)}_{\mu\tau}$.

The coefficient $\mathring{a}^{(3)}_{e\mu}$ is not shown separately in figures 8 and 9. The examples $\mathring{a}^{(3)}_{\mu\tau}$ and $\mathring{a}^{(3)}_{e\tau}$ illustrate the strongest and weakest sensitivity observed among the off-diagonal LIV coefficients, with the sensitivity to $\mathring{a}^{(3)}_{e\mu}$ being in between these two cases. Since $\mathring{a}^{(3)}_{e\mu}$ introduces oscillations between flavours that contribute to both the track-like and shower-like event classes, one might expect a sensitivity similar to that of $\mathring{a}^{(3)}_{\mu\tau}$. However, the matter potential experienced by electron neutrinos modifies the $\nu_e \leftrightarrow \nu_\mu$ oscillation pattern in a way that reduces the sensitivity to $\mathring{a}^{(3)}_{e\mu}$. Nevertheless, measurable distortions of the ν_μ survival probability appear for smaller values of $\mathring{a}^{(3)}_{e\mu}$ than for $\mathring{a}^{(3)}_{e\tau}$, resulting in a stronger constraint.

For $\mathring{a}^{(3)}_{\mu\mu-\tau\tau}$, the LIV contribution most notably enhances the ν_μ survival probability for vertically upgoing neutrinos in the energy range from approximately 15 GeV to 40 GeV relative to the standard oscillation scenario. This enhancement increases the expected event rates in the HPT and LPT classes in the corresponding reconstructed energy and zenith-angle region. In the per-bin test-statistic maps in figure 9, a corresponding region of tension is visible in the track-like samples, indicating that the observed data contain fewer events than predicted by this excluded LIV hypothesis in that part of the analysis space.

In the case of $\mathring{c}^{(4)}_{\mu\mu-\tau\tau}$, the energy dependence of the LIV-induced oscillation phase shifts the oscillation probability modifications towards higher energies. At the 99% CL excluded

JCAP11(2026)012

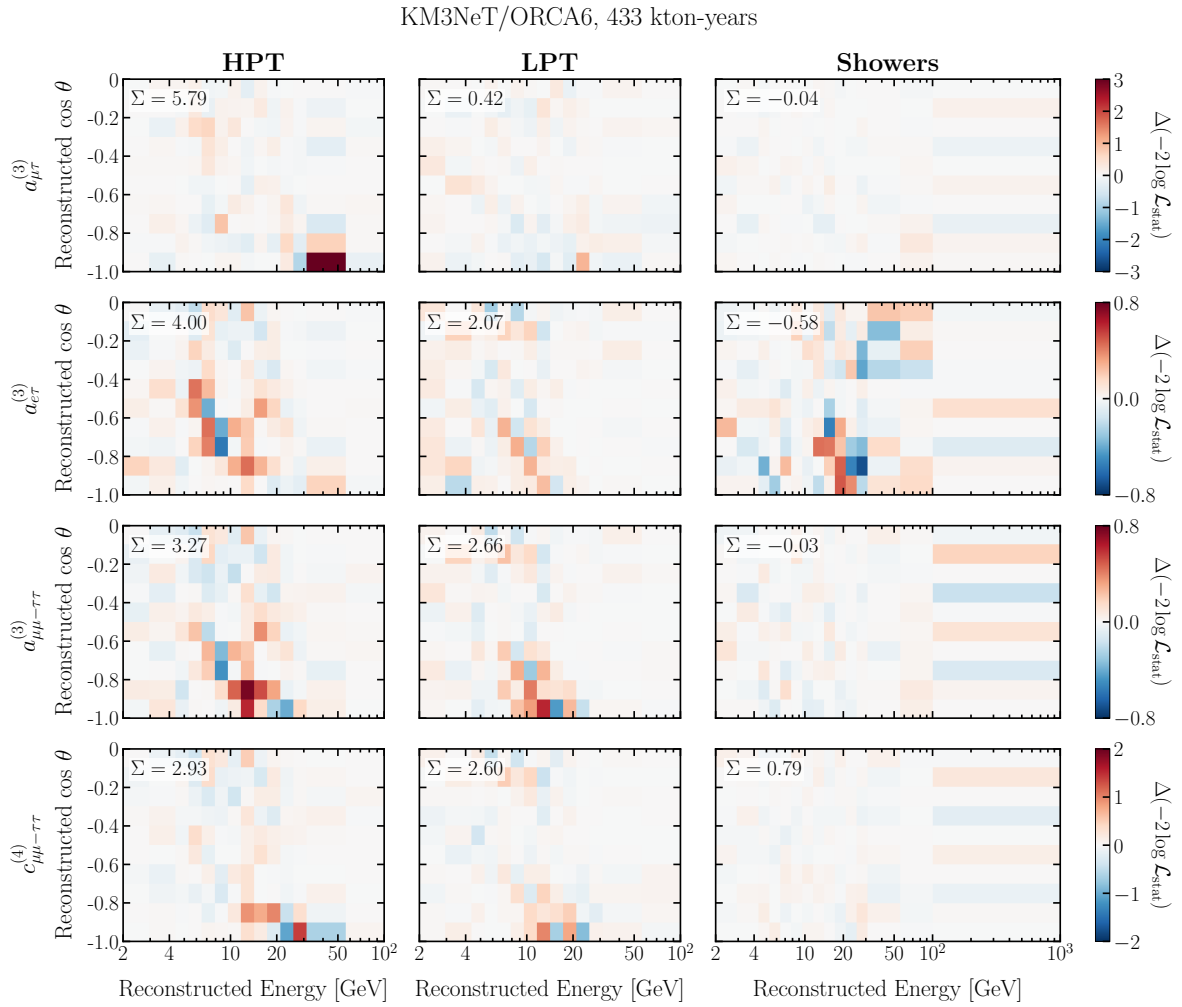


Figure 9. Per-bin differences in the statistical contribution to the log-likelihood, $\Delta(-2\log\mathcal{L}_{\text{stat}})$, between representative LIV hypotheses fixed to the corresponding 99% CL excluded values and the respective best-fit hypotheses. Here, $-2\log\mathcal{L}_{\text{stat}}$ denotes the likelihood defined in equation (5.1) without the nuisance parameter penalty terms. The rows correspond to the LIV coefficients indicated on the left-hand side, while the columns show the three particle-identification classes used in the analysis. The quantity Σ shown in each panel denotes the sum of the displayed per-bin contributions.

value shown in figure 8, the coefficient enhances the ν_μ survival probability for vertically upgoing neutrinos in the approximate $(20-100)$ GeV energy range. While this improves the agreement in the highest-statistics HPT bin, it simultaneously worsens the agreement in several neighbouring bins. The exclusion therefore arises not from a single dominant discrepancy, but from the combined tension across several high-energy bins of the HPT and LPT classes. Similar mechanisms are observed for the higher-dimensional diagonal coefficients, for which the sensitivity is driven primarily by distortions in the upper end of the oscillation-sensitive energy range accessible to the ORCA6 sample.

JCAP11(2026)012

6.4 Uncertainties in the nuisance parameters

Pull distributions for the same representative LIV coefficients discussed in section 6.3 are shown in figure 10. Additional pull distributions for the remaining coefficients are provided in appendix A. The distributions show that the fitted nuisance parameter values remain compatible with their nominal values within the assigned uncertainties. The largest pull is observed for the HPT normalisation parameter, which is shifted by about 2σ. This is compatible with the number of nuisance parameters considered in the fit, and no anomalously large displacement is observed. The fitted systematic pulls are similar across the different LIV fits, indicating that the inclusion of an individual LIV coefficient does not substantially shift the preferred values of the systematic parameters.

The fitted values of $\mathring{a}^{(3)}_{e\tau}$ and $\mathring{a}^{(3)}_{\mu\mu-\tau\tau}$ are particularly stable under nuisance parameter variations. For $\mathring{a}^{(3)}_{e\tau}$, the response to all considered nuisance parameter shifts is small compared to the post-fit LIV uncertainty. The coefficient $\mathring{a}^{(3)}_{\mu\mu-\tau\tau}$ shows a similarly weak dependence, with the largest response arising from a negative shift of θ_{23}.

For $\mathring{a}^{(3)}_{\mu\tau}$, the strongest dependence is observed for shifts of Δm^2_{31}. This can be understood from the fact that Δm^2_{31} sets the L/E scale of the standard atmospheric oscillation pattern. A shift in Δm^2_{31} therefore changes the energy at which the standard oscillation extrema occur, while a change in $\mathring{a}^{(3)}_{\mu\tau}$ can partially compensate the resulting mismatch by modifying the size of the LIV-induced deviations from the standard oscillation expectation.

For $\mathring{c}^{(4)}_{\mu\mu-\tau\tau}$, the largest response is observed for shifts of θ_{23}. This is plausible, since both parameters influence the amplitude of the first atmospheric $\nu_\mu \to \nu_\tau$ oscillation maximum. Changes in one parameter can therefore be partially compensated by changes in the other when fitting the observed event rates.

6.5 Goodness of fit and comparison to expected sensitivity

The goodness of fit was evaluated for three representative LIV coefficients using the same pseudo-experiment procedure as described in detail in the ORCA6 standard oscillation analysis [12]. For each pseudo-experiment, the full fit was repeated and the best-fit value of the likelihood $-2\log\mathcal{L}$ was used as the goodness-of-fit test statistic. The resulting test-statistic distributions are consistent with the distribution shown in figure 5 of the standard oscillation analysis. Given this consistency, and because the generation and refitting of pseudo-experiments is computationally expensive, no additional goodness-of-fit tests were performed for the remaining LIV coefficients.

The estimated p-values for the three representative LIV coefficients are 1.0% for $\mathring{a}^{(3)}_{\mu\tau}$, 1.2% for $\mathring{a}^{(3)}_{e\tau}$, and 1.1% for $\mathring{a}^{(3)}_{\mu\mu-\tau\tau}$. These values are compatible with the goodness of fit of $(1.20 \pm 0.15)\%$ reported for the standard oscillation analysis. This indicates that the inclusion of a single LIV coefficient does not substantially alter the goodness of fit of the ORCA6 data sample. A later fit of the standard oscillation hypothesis to a KM3NeT/ORCA dataset with more exposure, presented in [31], yields a p-value of 0.41, indicating improved agreement between data and expectation. Since this dataset has a large overlap with the ORCA6 sample, this supports the interpretation that the low goodness-of-fit value observed for ORCA6 was mainly driven by a statistical fluctuation.

JCAP11(2026)012

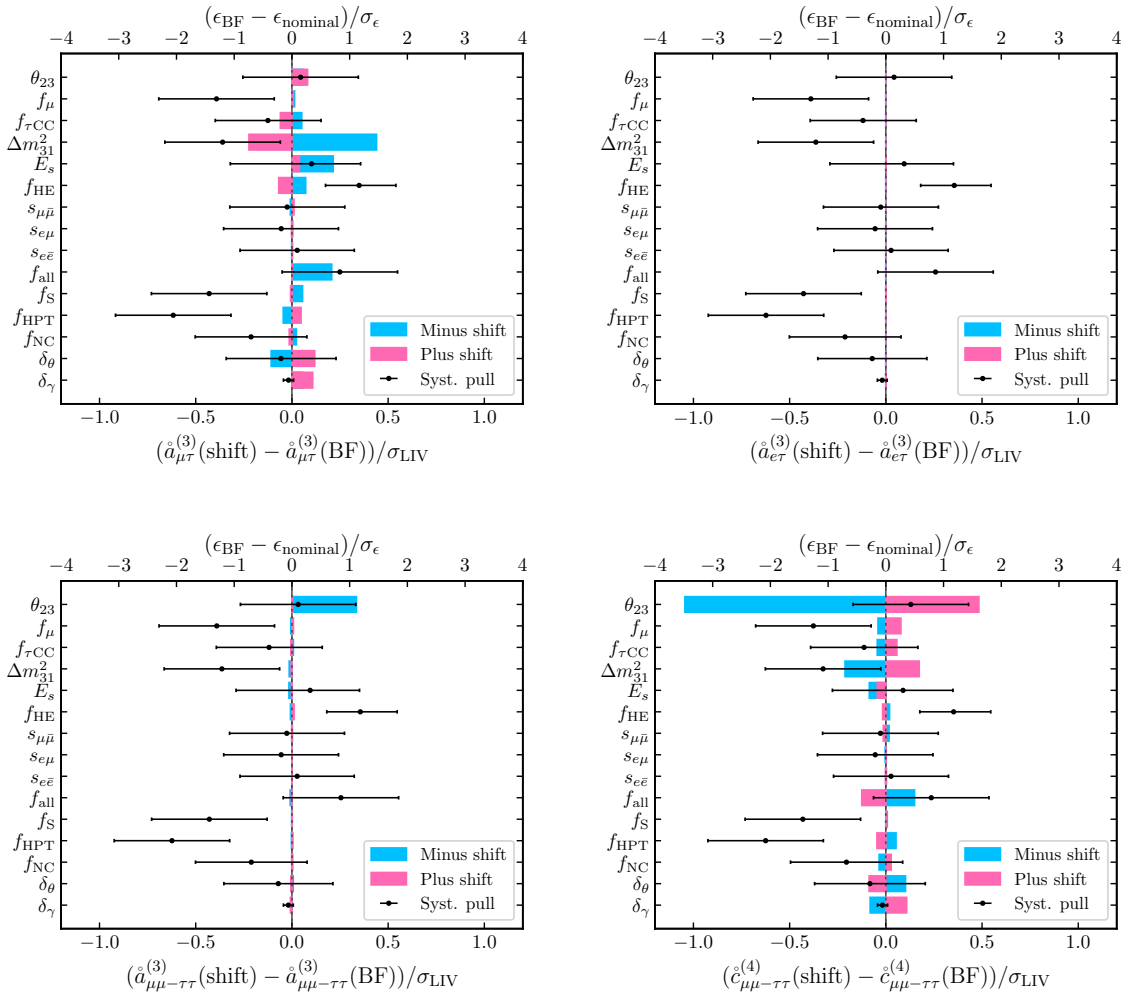


Figure 10. Pull distributions for representative LIV coefficients. The black points, read with respect to the top axis, show the fitted nuisance parameter values relative to their nominal values. For nuisance parameters with a pre-fit constraint, σ_ϵ denotes the corresponding prior uncertainty, while for unconstrained nuisance parameters the post-fit uncertainty is used instead. The horizontal error bars show the ratio of the post-fit to pre-fit uncertainty for constrained nuisance parameters and are set to unity for unconstrained parameters. The coloured bars, read with respect to the bottom axis, quantify the impact of individual nuisance parameters on the fitted LIV coefficient. The negative and positive shifts correspond to fixing the nuisance parameter to its post-fit -1σ and $+1\sigma$ values, respectively, while all remaining parameters are profiled. The fitted LIV coefficient obtained after each shift is compared to its nominal best-fit value, and the difference is normalised by the post-fit LIV uncertainty $\sigma_{\rm LIV}$.

The expected sensitivity was evaluated using 300 pseudo-experiments generated under the null hypothesis, i.e., standard oscillations. The pseudo-experiments were generated using the NuFit 5.0+SK normal-ordering oscillation parameters [29], with the nuisance parameters fixed to their nominal values. For each pseudo-experiment, likelihood-ratio scans were produced by fixing the LIV coefficient to each value considered in the scan and profiling all remaining fit

JCAP11(2026)012

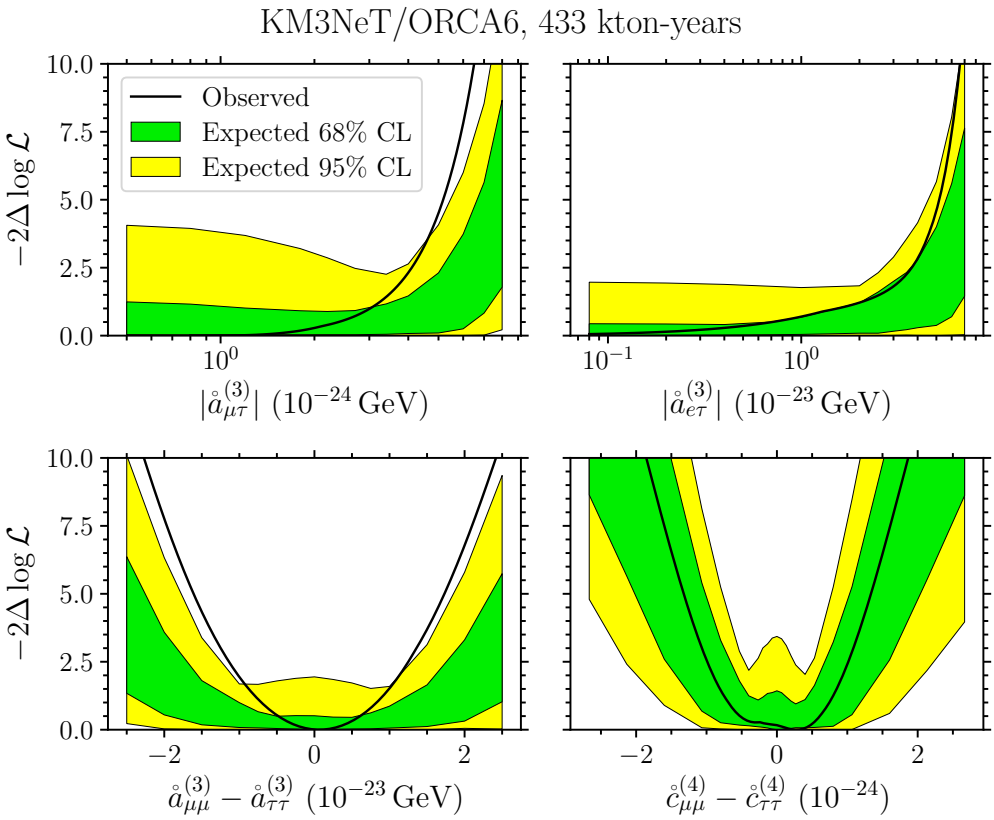


Figure 11. Expected sensitivity bands for representative LIV coefficients. The bands are obtained from 300 pseudo-experiments generated under the null hypothesis, corresponding to standard oscillations. For each fixed LIV-coefficient value, all remaining fit parameters are profiled. The green and yellow regions show the central 68% and 95% intervals of the expected test-statistic distributions, respectively. The black curves show the observed test-statistic scans obtained from data.

parameters. The resulting expected sensitivity bands are shown in figure 11 for the same representative LIV coefficients discussed in section 6.3.

For $\mathring{a}^{(3)}_{\mu\tau}$, the observed likelihood-ratio scan lies outside the central 95% expected interval over a part of the parameter range, indicating that the obtained constraint is stronger than expected under the null hypothesis. Figure 9 shows that most of this tension is concentrated in a single bin of the HPT class. This bin has the highest statistics in the analysis, containing 79 observed high-energy, vertically-upgoing events. It exhibits a mild excess with respect to the null hypothesis. To quantify the significance of this excess, we use the value of the per-bin test statistic $-2\log\mathcal{L}_{\mathrm{stat}}$ obtained from the fit to the null hypothesis, shown in the bottom row of figure 4. By Wilks' theorem [27], this test statistic approximately follows a χ^2 distribution with one degree of freedom, i.e., the distribution of Z^2 for a standard normally distributed variable Z. Evaluating $\sqrt{-2\log\mathcal{L}_{\mathrm{stat}}} \approx 1.6$ therefore quantifies this bin's deviation as an approximately $1.6\,\sigma$ excess with respect to the null-hypothesis expectation. This mild excess is the primary driver of the stronger-than-expected result, since $\mathring{a}^{(3)}_{\mu\tau}$ predicts a deficit of track-like events at the highest energies, as shown in figure 8. To quantify the impact of this bin, the fit was repeated with this single bin excluded from the HPT class.

JCAP11(2026)012

The resulting constraints at 95% (99%) CL are relaxed by 22.1% (19.2%) relative to the constraints obtained using all bins, and fall well within the expected region shown in figure 11, demonstrating that the tighter-than-expected constraints originate predominantly from the mild excess in this single bin.

The observed likelihood-ratio curve of $\mathring{a}^{(3)}_{\mu\mu-\tau\tau}$ also lies outside the central 95% expected interval over a part of the parameter range. As shown in figure 9, a significant fraction of the tension introduced by this coefficient is concentrated in three neighboring bins of the HPT class: $E_{\mathrm{reco}} \in [14.1, 17.2)\,\mathrm{GeV}$ with $\cos\theta_{\mathrm{reco}} \in [-0.9, -0.8)$, and $E_{\mathrm{reco}} \in [11.6, 14.1)\,\mathrm{GeV}$ with $\cos\theta_{\mathrm{reco}} \in [-1.0, -0.8)$. Note that the latter range covers two bins. Each of these three bins has a mild deficit with respect to the null hypothesis, which can be quantified as $1.0\,\sigma$, $0.5\,\sigma$, and $1.4\,\sigma$ underfluctuations using the same test statistic as in the previous discussion for $\mathring{a}^{(3)}_{\mu\tau}$. As shown in figure 8, $\mathring{a}^{(3)}_{\mu\mu-\tau\tau}$ predicts an excess of track-like events in this region of phase space, which is in tension with the mild deficit observed in these three bins, resulting in constraints that are tighter than expected. To quantify this, the fit was repeated with these three bins excluded from the HPT class. The resulting constraints for positive values of $\mathring{a}^{(3)}_{\mu\mu-\tau\tau}$ at 95% (99%) CL are relaxed by 18.3% (18.1%) relative to the constraints obtained using all bins and are within the expected 95% sensitivity region shown in figure 11. Analogously, the constraints for negative values of $\mathring{a}^{(3)}_{\mu\mu-\tau\tau}$ are relaxed by 16.1% (16.0%) and are also within the 95% expected sensitivity region.

For $\mathring{a}^{(3)}_{e\tau}$, the observed scan is compatible with the expected sensitivity bands. This is consistent with the fact that the regions of the analysis space driving the constraint are different from those relevant for $\mathring{a}^{(3)}_{\mu\tau}$ and $\mathring{a}^{(3)}_{\mu\mu-\tau\tau}$. As discussed in section 6.3, the sensitivity arises from distortions of the ν_μ survival probability around $E \sim 10\,\mathrm{GeV}$ and $\cos\theta \sim -0.6$, rather than from vertically upgoing events.

The observed scan for $\mathring{c}^{(4)}_{\mu\mu-\tau\tau}$ is also compatible with the expected sensitivity bands. Compared to $\mathring{a}^{(3)}_{\mu\mu-\tau\tau}$, the enhancement of the ν_μ survival probability is shifted towards higher energies for this coefficient. Consequently, the exclusion of $\mathring{c}^{(4)}_{\mu\mu-\tau\tau}$ is driven by different regions of the analysis space than the exclusion of $\mathring{a}^{(3)}_{\mu\mu-\tau\tau}$, which makes it plausible that the corresponding constraint remains within the expected sensitivity bands, in contrast to $\mathring{a}^{(3)}_{\mu\mu-\tau\tau}$.

6.6 Comparison with other experiments

In figure 12, the results of this analysis are compared with limits obtained from approximately 12 years of Super-Kamiokande data [8] and from a two-year IceCube analysis using atmospheric neutrinos [9]. Despite the small detector size and shorter livetime of ORCA6, the present analysis provides competitive constraints on the mass-dimension-three off-diagonal coefficients. Constraints on related isotropic LIV coefficients have also been reported by IceCube using high-energy astrophysical neutrinos [10]. However, those results depend strongly on the assumed initial flavour composition at the source, and for several plausible flavour ratios no upper limit could be established. They are therefore not included in figure 12.

The ORCA6 results provide the first direct constraints on isotropic flavour-diagonal LIV coefficient differences between the muon and tau sectors. In contrast to constraints derived from astrophysical flavour-composition measurements, these limits do not rely on

JCAP11(2026)012

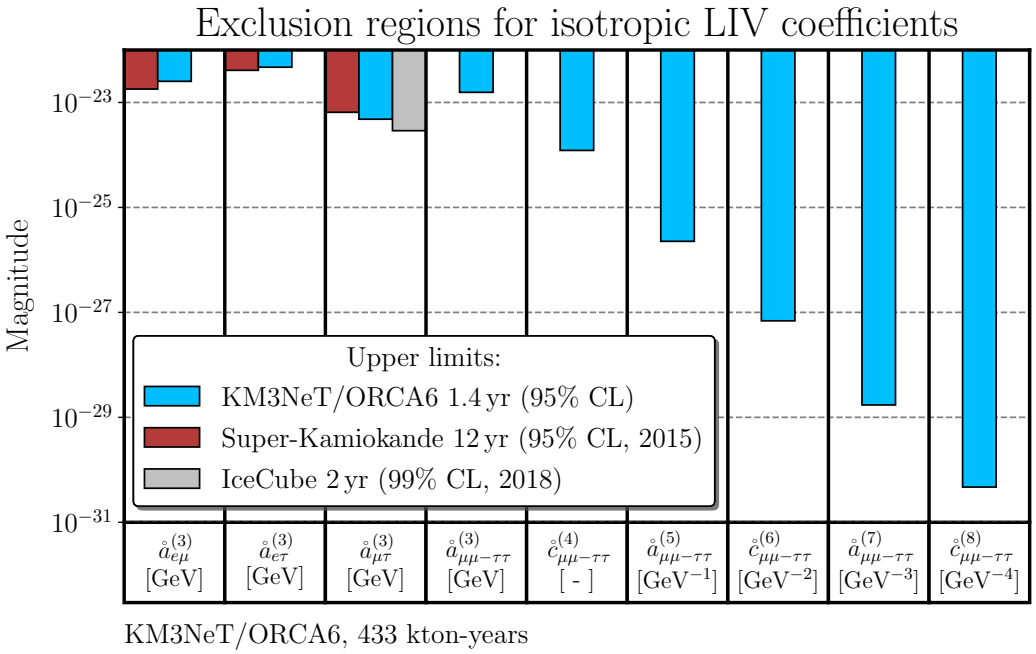


Figure 12. Exclusion regions for isotropic LIV coefficients obtained with 1.4 years of ORCA6 data. The regions are compared to previous upper limits set with 12 years of Super-Kamiokande data [8] and 2 years of IceCube data [9].

assumptions about the initial flavour composition at astrophysical neutrino sources, enhancing the robustness and general applicability of the constraints obtained in this analysis.

7 Conclusion

A search for isotropic Lorentz invariance violation was performed using 1.4 years of atmospheric neutrino data collected with the first six detection units of the KM3NeT/ORCA detector. No evidence for LIV was observed, and upper limits were therefore set on a subset of isotropic LIV coefficients. For the off-diagonal mass-dimension-three coefficients, the resulting constraints are competitive with existing limits from Super-Kamiokande and IceCube, despite the shorter livetime and small detector configuration.

In addition, the analysis provides the first direct constraints on isotropic flavour-diagonal LIV coefficient differences between the muon and tau sectors for mass dimensions $d = 3$ to 8. In contrast to constraints derived from astrophysical flavour-composition measurements, these limits do not rely on assumptions about the initial flavour composition at astrophysical neutrino sources. This independence from astrophysical source modelling enhances the robustness and general applicability of the constraints obtained in this analysis.

The present work lays the foundation for future analyses with larger data samples and an extended detector configuration, which are expected to improve the potential to explore subleading effects and probe additional LIV scenarios.

JCAP11(2026)012

A Pull distributions

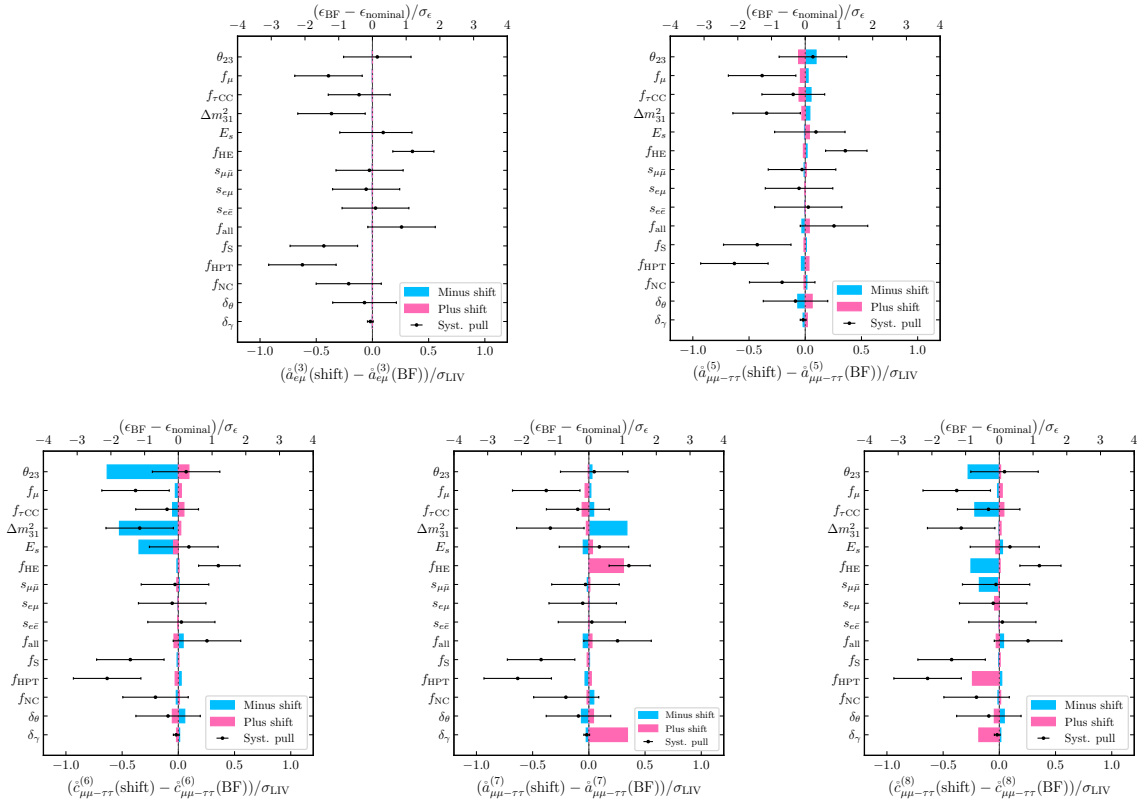


Figure 13. Additional pull distributions for LIV coefficients not shown in figure 10. The upper row shows $\mathring{a}^{(3)}_{e\mu}$ and the flavour-diagonal difference between the muon and tau sectors for mass dimension 5, while the lower row shows the corresponding flavour-diagonal differences for mass dimensions 6 to 8. The black points, horizontal error bars, and coloured bars are defined as in figure 10.

Acknowledgments

A. Domi acknowledges the support from the European Union's Horizon 2021 research and innovation programme under the Marie Skłodowska-Curie grant agreement No. 101068013 (QGRANT), and from the Emerging Talent Initiative funding at the Friedrich-Alexander-Universität Erlangen-Nürnberg. The authors acknowledge the financial support of: KM3NeT-INFRADEV2 project, funded by the European Union Horizon Europe Research and Innovation Programme under grant agreement No. 101079679; Funds for Scientific Research (FRS-FNRS), Francqui foundation, BAEF foundation. Czech Science Foundation (GAČR 24-12702S); Agence Nationale de la Recherche (contract ANR-15-CE31-0020), Centre National de la Recherche Scientifique (CNRS), Commission Européenne (FEDER fund and Marie Curie Program), LabEx UnivEarthS (ANR-10-LABX-0023 and ANR-18-IDEX-0001), Paris Île-de-France Region, Normandy Region (Alpha, Blue-waves and Neptune), France, The Provence-Alpes-Côte d'Azur Delegation for Research and Innovation (DRARI), the Provence-Alpes-Côte d'Azur region, the Bouches-du-Rhône Departmental Council, the Metropolis of

JCAP11(2026)012

Aix-Marseille Provence and the City of Marseille through the CPER 2021-2027 NEUMED project, The CNRS Institut National de Physique Nucléaire et de Physique des Particules (IN2P3); Shota Rustaveli National Science Foundation of Georgia (SRNSFG, FR-22-13708), Georgia. This research was funded by the European Union (ERC MuSES project No 101142396); The General Secretariat of Research and Innovation (GSRI), Greece; Istituto Nazionale di Fisica Nucleare (INFN) and Ministero dell'Università e della Ricerca (MUR), through PRIN 2022 program (Grant PANTHEON 2022E2J4RK, Next Generation EU) and PON R&I program (Avviso n. 424 del 28 febbraio 2018, Progetto PACK-PIR01 00021), Italy; IDMAR project Po-Fesr Sicilian Region az. 1.5.1; A. De Benedittis, W. Idrissi Ibnsalih, M. Bendahman, A. Nayerhoda, G. Papalashvili, I. C. Rea, A. Simonelli have been supported by the Italian Ministero dell'Università e della Ricerca (MUR), Progetto CIR01 00021 (Avviso n. 2595 del 24 dicembre 2019); KM3NeT4RR MUR Project National Recovery and Resilience Plan (NRRP), Mission 4 Component 2 Investment 3.1, Funded by the European Union — NextGenerationEU,CUP I57G21000040001, Concession Decree MUR No. n. Prot. 123 del 21/06/2022; Ministry of Higher Education, Scientific Research and Innovation, Morocco, and the Arab Fund for Economic and Social Development, Kuwait; Nederlandse organisatie voor Wetenschappelijk Onderzoek (NWO), the Netherlands; The grant "AstroCeNT: Particle Astrophysics Science and Technology Centre", carried out within the International Research Agendas programme of the Foundation for Polish Science financed by the European Union under the European Regional Development Fund; The program: "Excellence initiative-research university" for the AGH University in Krakow; The ARTIQ project: UMO-2021/01/2/ST6/00004 and ARTIQ/0004/2021; Ministry of Education and Scientific Research, Romania Slovak Research and Development Agency under Contract No. APVV-22-0413; Ministry of Education, Research, Development and Youth of the Slovak Republic; MCIN for PID2021-124591NB-C41, -C42, -C43 and PDC2023-145913-I00 funded by MCIN/AEI/10.13039/501100011033 and by "ERDF A way of making Europe", for ASFAE/2022/014 and ASFAE/2022 /023 with funding from the EU NextGenerationEU (PRTR-C17.I01) and Generalitat Valenciana, for Grant AST22_6.2 with funding from Consejería de Universidad, Investigación e Innovación and Gobierno de España and European Union - NextGenerationEU, for CSIC-INFRA23013 and for CNS2023-144099, Generalitat Valenciana for CIDEGENT/2020/049, CIDEGENT/2021/23, CIDEIG/2023/20, ESGENT2024/24, CIPROM/2023/51, GRISOLIAP/2021/192 and INNVA1/2024/110 (IVACE+i), Spain; Khalifa University internal grants (ESIG-2023-008, RIG-2023-070 and RIG-2024-047), United Arab Emirates; The European Union's Horizon 2020 Research and Innovation Programme (ChETEC-INFRA - Project no. 101008324). Views and opinions expressed are those of the author(s) only and do not necessarily reflect those of the European Union or the European Research Council. Neither the European Union nor the granting authority can be held responsible for them.

References

[1] H. Vucetich, *Testing Lorentz invariance violation in quantum gravity theories*, gr-qc/0502093 [INSPIRE].

JCAP11(2026)012

[2] C. Li and B.-Q. Ma, *Lorentz- and CPT-violating neutrinos from string/D-brane model*, *Phys. Lett. B* **835** (2022) 137543 [arXiv:2211.00900] [INSPIRE].

[3] J. Alfaro, M. Reyes, H.A. Morales-Tecotl and L.F. Urrutia, *On alternative approaches to Lorentz violation invariance in loop quantum gravity inspired models*, *Phys. Rev. D* **70** (2004) 084002 [gr-qc/0404113] [INSPIRE].

[4] G. Amelino-Camelia, J. Kowalski-Glikman, G. Mandanici and A. Procaccini, *Phenomenology of doubly special relativity*, *Int. J. Mod. Phys. A* **20** (2005) 6007 [gr-qc/0312124] [INSPIRE].

[5] S.M. Carroll et al., *Noncommutative field theory and Lorentz violation*, *Phys. Rev. Lett.* **87** (2001) 141601 [hep-th/0105082] [INSPIRE].

[6] V.A. Kostelecky, R. Lehnert and M.J. Perry, *Spacetime-varying couplings and Lorentz violation*, *Phys. Rev. D* **68** (2003) 123511 [astro-ph/0212003] [INSPIRE].

[7] A. Kostelecky and M. Mewes, *Neutrinos with Lorentz-violating operators of arbitrary dimension*, *Phys. Rev. D* **85** (2012) 096005 [arXiv:1112.6395] [INSPIRE].

[8] Super-Kamiokande collaboration, *Test of Lorentz invariance with atmospheric neutrinos*, *Phys. Rev. D* **91** (2015) 052003 [arXiv:1410.4267] [INSPIRE].

[9] IceCube collaboration, *Neutrino Interferometry for High-Precision Tests of Lorentz Symmetry with IceCube*, *Nature Phys.* **14** (2018) 961 [arXiv:1709.03434] [INSPIRE].

[10] IceCube collaboration, *Search for quantum gravity using astrophysical neutrino flavour with IceCube*, *Nature Phys.* **18** (2022) 1287 [arXiv:2111.04654] [INSPIRE].

[11] KM3NeT collaboration, *Letter of intent for KM3NeT 2.0*, *J. Phys. G* **43** (2016) 084001 [arXiv:1601.07459] [INSPIRE].

[12] KM3NeT collaboration, *Measurement of neutrino oscillation parameters with the first six detection units of KM3NeT/ORCA*, *JHEP* **10** (2024) 206 [*Addendum ibid.* **10** (2025) 041] [arXiv:2408.07015] [INSPIRE].

[13] V.A. Kostelecky, C.D. Lane and A.G.M. Pickering, *One loop renormalization of Lorentz violating electrodynamics*, *Phys. Rev. D* **65** (2002) 056006 [hep-th/0111123] [INSPIRE].

[14] C. Giunti and C.W. Kim, *Fundamentals of Neutrino Physics and Astrophysics*, Oxford University Press (2007) [DOI:10.1093/acprof:oso/9780198508717.001.0001] [INSPIRE].

[15] KM3NeT collaboration, *Search for non-standard neutrino interactions with the first six detection units of KM3NeT/ORCA*, *JCAP* **02** (2025) 073 [arXiv:2411.19078] [INSPIRE].

[16] G. Barenboim, M. Masud, C.A. Ternes and M. Tórtola, *Exploring the intrinsic Lorentz-violating parameters at DUNE*, *Phys. Lett. B* **788** (2019) 308 [arXiv:1805.11094] [INSPIRE].

[17] S.K. Agarwalla, S. Das, S. Sahoo and P. Swain, *Constraining Lorentz invariance violation with next-generation long-baseline experiments*, *JHEP* **07** (2023) 216 [arXiv:2302.12005] [INSPIRE].

[18] J. Coelho et al., *OscProb*, https://doi.org/10.5281/zenodo.17651666 (2025).

[19] KM3NeT collaboration, *The KM3NeT multi-PMT optical module*, 2022 *JINST* **17** P07038 [arXiv:2203.10048] [INSPIRE].

[20] KM3NeT collaboration, *Search for an eV-scale sterile neutrino with the first six detection units of KM3NeT/ORCA*, *JHEP* **02** (2026) 080 [arXiv:2510.07360] [INSPIRE].

[21] KM3NeT collaboration, *Search for quantum decoherence in neutrino oscillations with six detection units of KM3NeT/ORCA*, *JCAP* **03** (2025) 039 [arXiv:2410.01388] [INSPIRE].

JCAP11(2026)012

[22] KM3NeT collaboration, *Probing invisible neutrino decay with the first six detection units of KM3NeT/ORCA*, *JHEP* **04** (2025) 105 [arXiv:2501.11336] [INSPIRE].

[23] KM3NeT collaboration, *Study of tau neutrinos and non-unitary neutrino mixing with the first six detection units of KM3NeT/ORCA*, *JHEP* **07** (2025) 213 [arXiv:2502.01443] [INSPIRE].

[24] R.J. Barlow and C. Beeston, *Fitting using finite Monte Carlo samples*, *Comput. Phys. Commun.* **77** (1993) 219 [INSPIRE].

[25] J.S. Conway, *Incorporating Nuisance Parameters in Likelihoods for Multisource Spectra*, in the proceedings of the *PHYSTAT 2011*, Geneva, Switzerland, 17–20 January (2011) [DOI:10.5170/CERN-2011-006.115] [arXiv:1103.0354] [INSPIRE].

[26] F. James, *MINUIT Function Minimization and Error Analysis: Reference Manual Version 94.1*, CERN-D-506 (1994) [INSPIRE].

[27] S.S. Wilks, *The Large-Sample Distribution of the Likelihood Ratio for Testing Composite Hypotheses*, *Annals Math. Statist.* **9** (1938) 60 [INSPIRE].

[28] G.J. Feldman and R.D. Cousins, *A unified approach to the classical statistical analysis of small signals*, *Phys. Rev. D* **57** (1998) 3873 [physics/9711021] [INSPIRE].

[29] I. Esteban et al., *The fate of hints: updated global analysis of three-flavor neutrino oscillations*, *JHEP* **09** (2020) 178 [arXiv:2007.14792] [INSPIRE].

[30] M. Honda et al., *Atmospheric neutrino flux calculation using the NRLMSISE-00 atmospheric model*, *Phys. Rev. D* **92** (2015) 023004 [arXiv:1502.03916] [INSPIRE].

[31] J. Coelho, *Latest results from KM3NeT*, https://agenda.infn.it/event/37867/contributions/233917/ (2024).

JCAP11(2026)012

The KM3NeT collaboration

O. Adriani[b,a], A. Albert[c,bf], A.R. Alhebsi[d], S. Alshalloudi[d], S. Alves Garre[e], F. Ameli[f], M. Andre[g], L. Aphecetche[h], M. Ardid[i], S. Ardid[i], J. Aublin[j], F. Badaracco[l,k], L. Bailly-Salins[m], B. Baret[j], A. Bariego-Quintana[e], L. Barigione[k,l], M. Barnard[n], Y. Becherini[j], M. Bendahman[o], F. Benfenati Gualandi[q,p], M. Benhassi[r,o], D.M. Benoit[s], Z. Beňušová[u,t], E. Berbee[v], C. van Bergen[v], E. Berti[b], V. Bertin[w], P. Betti[b], S. Biagi[x], M. Boettcher[n], D. Bonanno[x], M. Bondì[y], M. Bongi[a,b], S. Bottai[b], A.B. Bouasla[bg], J. Boumaaza[z], M. Bouta[w], C. Bozza[aa,o], R.M. Bozza[ab,o], H. Brânzaş[ac], F. Bretaudeau[h], M. Breuhaus[w], R. Bruijn[ad,v], J. Brunner[w], R. Bruno[y], E. Buis[v], R. Buompane[r,o], I. Burriel[e], J. Busto[w], B. Caiffi[l], D. Calvo[e], E.G.J. van Campenhout[v], A. Capone[f,ae], F. Carenini[q,p], V. Carretero[ad,v], T. Cartraud[j], P. Castaldi[af,p], V. Cecchini[e], S. Celli[f,ae], M. Chabab[ag], A. Chen[ah], S. Cherubini[ai,x], T. Chiarusi[p], W. Chung[aj], M. Circella[ak], R. Clark[al], R. Cocimano[x], J.A.B. Coelho[j], A. Coleiro[j], A. Condorelli[j], R. Coniglione[x], P. Coyle[w], A. Creusot[j], G. Cuttone[x], R. Dallier[h], A. De Benedittis[r,o], X. de La Bernardie[h], G. De Wasseige[al], V. Decoene[h], P. Deguire[w], I. Del Rosso[q,p], L.S. Di Mauro[x], I. Di Palma[f,ae], A.F. Díaz[am], D. Diego-Tortosa[bh,x], C. Distefano[x], A. Domi[an,1], C. Donzaud[j], D. Dornic[w], E. Drakopoulou[ao], D. Drouhin[c,bf], J.-G. Ducoin[w], P. Duverne[j], R. Dvornický[u], T. Eberl[an], E. Eckerová[u,t], A. Eddymaoui[z], M. Eff[j], D. van Eijk[v], I. El Bojaddaini[ap], S. El Hedri[j], S. El Mentawi[w], V. Ellajosyula[l], A. Enzenhöfer[w], M. Farino[aj], A. Ferrara[aq,o], G. Ferrara[ai,x], M.D. Filipović[ar], F. Filippini[p], A. Foisseau[w], D. Franciotti[x], L.A. Fusco[aa,o], S. Gagliardini[ae,f], T. Gal[an], J. García Méndez[i], A. Garcia Soto[e], C. Gatius Oliver[v], N. Geißelbrecht[an], H. Ghaddari[ap], L. Gialanella[r,o], B.K. Gibson[s], E. Giorgio[x], I. Goos[j], P. Goswami[j], S.R. Gozzini[e], R. Gracia[an], B. Guillon[m], C. Haack[an], C. Hanna[aj], H. van Haren[as], E. Hazelton[aj], A. Heijboer[v], L. Hennig[an,1], J.J. Hernández-Rey[e], A. Idrissi[x], W. Idrissi Ibnsalih[o], G. Illuminati[p], R. Jaimes[e], O. Janik[an], D. Joly[w], M. de Jong[at,v], P. de Jong[ad,v], B.J. Jung[v], P. Kalaczyński[bi,au], T. Kapoor[av], U.F. Katz[an], J. Keegans[s], T. Khvichia[aw], G. Kistauri[ax,aw], C. Kopper[an], A. Kouchner[ay,j], Y.Y. Kovalev[az], L. Krupa[t], V. Kueviakoe[v], V. Kulikovskiy[l], R. Kvatadze[ax], M. Labalme[m], R. Lahmann[an], M. Lamoureux[j], A. Langella[aj], G. Larosa[x], C. Lastoria[m], J. Lazar[al], A. Lazo[e], G. Lehaut[m], V. Lemaître[al], E. Leonora[y], N. Lessing[e], G. Levi[q,p], M. Lindsey Clark[j], F. Longhitano[y], M. Loup[j], A. Luashvili[n], S. Madarapu[e], F. Magnani[w], L. Malerba[l,k], F. Mamedov[t], A. Manfreda[o], A. Manousakis[ba], M. Marconi[k,l], A. Margiotta[q,p], A. Marinelli[ab,o], C. Markou[ao], L. Martin[h], M. Mastrodicasa[ae,f], S. Mastroianni[o], J. Mauro[al], K.C.K. Mehta[au], G. Miele[ab,o], P. Migliozzi[o], E. Migneco[x], M.L. Mitsou[r,o], C.M. Mollo[o], L. Morales-Gallegos[r,o], N. Mori[b], A. Moussa[ap], I. Mozun Mateo[m], R. Muller[p], M.R. Musone[r,o], M. Musumeci[x], S. Navas[bb], A. Nayerhoda[ak], C.A. Nicolau[f], B. Nkosi[ah], B. Ó Fearraigh[l], V. Oliviero[ab,o], A. Orlando[x], E. Oukacha[j], L. Pacini[a,b], D. Paesani[x], J. Palacios González[e], G. Papalashvili[ak,aw], P. Papini[b], V. Parisi[k,l], A. Parmar[m], G. Pascua[e], B. Pascual-Estrugo[i], C. Pastore[ak], A. M. Păun[ac], G.E. Păvălaş[ac], S. Peña Martínez[j], M. Perrin-Terrin[w], V. Pestel[m], M. Petropavlova[t,bj], P. Piattelli[x], A. Plavin[az,bk], C. Poirè[aa,o], T. Pradier[c], J. Prado[e], S. Pulvirenti[x], N. Randazzo[y], A. Ratnani[bc], S. Razzaque[bd], I.C. Rea[o], D. Real[e], G. Riccobene[x], J. Robinson[n], A. Romanov[m], E. Ros[az], A. Šaina[e], F. Salesa Greus[e], D.F.E. Samtleben[at,v], A. Sánchez Losa[e], S. Sanfilippo[x], M. Sanguineti[k,l],

JCAP11(2026)012

D. Santonocito[x], P. Sapienza[x], M. Scaringella[b], M. Scarnera[al,j], J. Schnabel[an], J. Schumann[an], M. Senniappan[d], P.A. Sevle Myhr[al], I. Sgura[ak], R. Shanidze[aw], C. Shao[bl,w], A. Sharma[j], Y. Shitov[t], F. Šimkovic[u], A. Simonelli[o], A. Sinopoulou[y], C. Sironneau[w], B. Spisso[o], M. Spurio[q,p], O. Starodubtsev[b], I. Štekl[t], D. Stocco[h], M. Taiuti[k,l], Y. Tayalati[z,bc], J. Tena[e], H. Thiersen[n], S. Thoudam[d], I. Tosta e Melo[y,ai], B. Trocmé[j], V. Tsourapis[ao], C. Tully[aj], E. Tzamariudaki[ao], A. Ukleja[au], A. Vacheret[m], V. Valsecchi[x], V. Van Elewyck[ay,j], G. Vannoye[k,l], E. Vannuccini[b], G. Vasileiadis[be], F. Vazquez de Sola[v], A. Veutro[f,ae], S. Viola[x], D. Vivolo[r,o], A. van Vliet[d], L. Voorend[at], E. de Wolf[ad,v], I. Lhenry-Yvon[j], S. Zavatarelli[l], D. Zito[x], J.D. Zornoza[e], J. Zúñiga[e]

[a] *Università di Firenze, Dipartimento di Fisica e Astronomia, via Sansone 1, Sesto Fiorentino, 50019 Italy*
[b] *INFN, Sezione di Firenze, via Sansone 1, Sesto Fiorentino, 50019 Italy*
[c] *Université de Strasbourg, CNRS, IPHC UMR 7178, F-67000 Strasbourg, France*
[d] *Khalifa University of Science and Technology, Department of Physics, PO Box 127788, Abu Dhabi, United Arab Emirates*
[e] *IFIC - Instituto de Física Corpuscular (CSIC - Universitat de València), Catedrático José Beltrán, 2, 46980 Paterna, Valencia, Spain*
[f] *INFN, Sezione di Roma, Piazzale Aldo Moro, 2 - c/o Dipartimento di Fisica, Edificio, G. Marconi, Roma, 00185 Italy*
[g] *Universitat Politècnica de Catalunya, Laboratori d'Aplicacions Bioacústiques, Centre Tecnològic de Vilanova i la Geltrú, Avda. Rambla Exposició, s/n, Vilanova i la Geltrú, 08800 Spain*
[h] *Subatech, IMT Atlantique, IN2P3-CNRS, Nantes Université, 4 rue Alfred Kastler - La Chantrerie, Nantes, BP 20722 44307 France*
[i] *Universitat Politècnica de València, Instituto de Investigación para la Gestión Integrada de las Zonas Costeras, C/ Paranimf, 1, Gandia, 46730 Spain*
[j] *Université Paris Cité, CNRS, Astroparticule et Cosmologie, F-75013 Paris, France*
[k] *Università di Genova, Via Dodecaneso 33, Genova, 16146 Italy*
[l] *INFN, Sezione di Genova, Via Dodecaneso 33, Genova, 16146 Italy*
[m] *LPC CAEN, Normandie Univ, ENSICAEN, UNICAEN, CNRS/IN2P3, 6 boulevard Maréchal Juin, Caen, 14050 France*
[n] *North-West University, Centre for Space Research, Private Bag X6001, Potchefstroom, 2520 South Africa*
[o] *INFN, Sezione di Napoli, Complesso Universitario di Monte S. Angelo, Via Cintia ed. G, Napoli, 80126 Italy*
[p] *INFN, Sezione di Bologna, v.le C. Berti-Pichat, 6/2, Bologna, 40127 Italy*
[q] *Università di Bologna, Dipartimento di Fisica e Astronomia, v.le C. Berti-Pichat, 6/2, Bologna, 40127 Italy*
[r] *Università degli Studi della Campania "Luigi Vanvitelli", Dipartimento di Matematica e Fisica, viale Lincoln 5, Caserta, 81100 Italy*
[s] *E.A. Milne Centre for Astrophysics, University of Hull, Hull, HU6 7RX, United Kingdom*
[t] *Czech Technical University in Prague, Institute of Experimental and Applied Physics, Husova 240/5, Prague, 110 00 Czech Republic*

JCAP11(2026)012

[u] Comenius University in Bratislava, Department of Nuclear Physics and Biophysics,
Mlynska dolina F1, Bratislava, 842 48 Slovak Republic
[v] Nikhef, National Institute for Subatomic Physics,
PO Box 41882, Amsterdam, 1009 DB The Netherlands
[w] Aix Marseille Univ, CNRS/IN2P3, CPPM,
Marseille, France
[x] INFN, Laboratori Nazionali del Sud,
(LNS) Via S. Sofia 62, Catania, 95123 Italy
[y] INFN, Sezione di Catania,
(INFN-CT) Via Santa Sofia 64, Catania, 95123 Italy
[z] University Mohammed V in Rabat, Faculty of Sciences,
4 av. Ibn Battouta, B.P. 1014, R.P. 10000 Rabat, Morocco
[aa] Università di Salerno e INFN Gruppo Collegato di Salerno, Dipartimento di Fisica,
Via Giovanni Paolo II 132, Fisciano, 84084 Italy
[ab] Università di Napoli "Federico II", Dip. Scienze Fisiche "E. Pancini",
Complesso Universitario di Monte S. Angelo, Via Cintia ed. G, Napoli, 80126 Italy
[ac] Institute of Space Science - INFLPR Subsidiary,
409 Atomistilor Street, Magurele, Ilfov, 077125 Romania
[ad] University of Amsterdam, Institute of Physics/IHEF,
PO Box 94216, Amsterdam, 1090 GE The Netherlands
[ae] Università La Sapienza, Dipartimento di Fisica,
Piazzale Aldo Moro 2, Roma, 00185 Italy
[af] Università di Bologna,
Dipartimento di Ingegneria dell'Energia Elettrica e dell'Informazione "Guglielmo Marconi",
Via dell'Università 50, Cesena, 47521 Italia
[ag] Cadi Ayyad University, Physics Department, Faculty of Science Semlalia,
Av. My Abdellah, P.O.B. 2390, Marrakech, 40000 Morocco
[ah] University of the Witwatersrand, School of Physics,
Private Bag 3, Johannesburg, Wits 2050 South Africa
[ai] Università di Catania, Dipartimento di Fisica e Astronomia "Ettore Majorana",
(INFN-CT) Via Santa Sofia 64, Catania, 95123 Italy
[aj] Princeton University, Department of Physics,
Jadwin Hall, Princeton, New Jersey, 08544 U.S.A.
[ak] INFN, Sezione di Bari,
via Orabona, 4, Bari, 70125 Italy
[al] UCLouvain, Centre for Cosmology, Particle Physics and Phenomenology,
Chemin du Cyclotron, 2, Louvain-la-Neuve, 1348 Belgium
[am] University of Granada, Department of Computer Engineering, Automation and Robotics / CITIC,
18071 Granada, Spain
[an] Friedrich-Alexander-Universität Erlangen-Nürnberg (FAU), Erlangen Centre for Astroparticle Physics,
Nikolaus-Fiebiger-Straße 2, 91058 Erlangen, Germany
[ao] NCSR Demokritos, Institute of Nuclear and Particle Physics,
Ag. Paraskevi Attikis, Athens, 15310 Greece
[ap] University Mohammed I, Faculty of Sciences,
BV Mohammed VI, B.P. 717, R.P. 60000 Oujda, Morocco
[aq] Università degli Studi della Campania "Luigi Vanvitelli", CAPACITY,
Laboratorio CIRCE - Dip. Di Matematica e Fisica,
Viale Carlo III di Borbone 153, San Nicola La Strada, 81020 Italy
[ar] Western Sydney University, School of Science,
Locked Bag 1797, Penrith, NSW 2751 Australia
[as] NIOZ (Royal Netherlands Institute for Sea Research),
PO Box 59, Den Burg, Texel, 1790 AB, The Netherlands
[at] Leiden University, Leiden Institute of Physics,

JCAP11(2026)012

PO Box 9504, Leiden, 2300 RA The Netherlands
[au] *AGH University of Krakow,*
Al. Mickiewicza 30, 30-059 Krakow, Poland
[av] *LPC, Campus des Cézeaux 24, avenue des Landais BP 80026, Aubière Cedex, 63171 France*
[aw] *Tbilisi State University, Department of Physics,*
3, Chavchavadze Ave., Tbilisi, 0179 Georgia
[ax] *The University of Georgia, Institute of Physics,*
Kostava str. 77, Tbilisi, 0171 Georgia
[ay] *Institut Universitaire de France,*
1 rue Descartes, Paris, 75005 France
[az] *Max-Planck-Institut für Radioastronomie,*
Auf dem Hügel 69, 53121 Bonn, Germany
[ba] *University of Sharjah, Sharjah Academy for Astronomy, Space Sciences, and Technology,*
University Campus - POB 27272, Sharjah, United Arab Emirates
[bb] *University of Granada, Dpto. de Física Teórica y del Cosmos & C.A.F.P.E.,*
18071 Granada, Spain
[bc] *School of Applied and Engineering Physics, Mohammed VI Polytechnic University,*
Ben Guerir, 43150, Morocco
[bd] *University of Johannesburg, Department Physics,*
PO Box 524, Auckland Park, 2006 South Africa
[be] *Laboratoire Univers et Particules de Montpellier,*
Place Eugène Bataillon - CC 72, Montpellier Cédex 05, 34095 France
[bf] *Université de Haute Alsace,*
rue des Frères Lumière, 68093 Mulhouse Cedex, France
[bg] *Université Badji Mokhtar, Département de Physique, Faculté des Sciences,*
Laboratoire de Physique des Rayonnements, B.P. 12, Annaba, 23000 Algeria
[bh] *CSIC - Consejo Superior de Investigaciones Cientificas, ICM-CSIC - Instituto de Ciencias del Mar,*
Paseo Maritimo de la Barceloneta, 37-49, Barcelona, 8003 Spain
[bi] *AstroCeNT, Nicolaus Copernicus Astronomical Center, Polish Academy of Sciences,*
Rektorska 4, Warsaw, 00-614 Poland
[bj] *Charles University, Faculty of Mathematics and Physics,*
Ovocný trh 5, Prague, 116 36 Czech Republic
[bk] *Harvard University, Black Hole Initiative,*
20 Garden Street, Cambridge, MA 02138 U.S.A.
[bl] *School of Physics and Astronomy, Sun Yat-sen University,*
Zhuhai, China

[1] *Corresponding author.*

JCAP11(2026)012